

Detecting young, slow-slipping active faults by geologic and multidisciplinary high-resolution geophysical investigations: a case study from the Apennine seismic belt, Italy

L. Improta¹, L. Ferranti², P.M. De Martini¹, S. Piscitelli³, P.P. Bruno⁴, P. Burrato¹, R. Civico¹, A. Giocoli³, M. Iorio⁵, G. D'Addezio¹, L. Maschio²

1. Istituto Nazionale di Geofisica e Vulcanologia, Sismologia e Tettonofisica, Rome, Italy
2. Dipartimento di Scienze della Terra, Università di Napoli, Federico II, Naples, Italy
3. Istituto di Metodologie per l'Analisi Ambientale, CNR, Marsico Nuovo, Potenza, Italy
4. Istituto Nazionale di Geofisica e Vulcanologia, Osservatorio Vesuviano, Naples, Italy
5. Istituto Ambiente Marino Costiero, CNR, Naples, Italy

Abstract

The Southern Apennines range of Italy presents significant challenges for active fault detection due to the complex structural setting inherited from previous contractional tectonics, coupled to very recent (Middle Pleistocene) onset and slow slip rates of active normal faults. As shown by the Irpinia Fault, source of a M6.9 earthquake in 1980, major faults might have small cumulative deformation and subtle geomorphic expression. A multidisciplinary study including morphological-tectonic, paleoseismological and geophysical investigations has been carried out across the extensional Monte Aquila Fault, a poorly known structure that, similarly to the Irpinia Fault, runs across a ridge and is weakly expressed at the surface by small scarps/warps. The joint application of shallow reflection profiling, seismic and electrical resistivity tomography, and physical logging of cored sediments has proved crucial for proper fault detection because performance of each technique was markedly different and very dependent on local geologic conditions. Geophysical data clearly: a) image a fault zone beneath suspected warps, b) constrain the cumulative vertical slip to only 25-30 m, c) delineate colluvial packages suggesting co-seismic surface faulting episodes.

27 Paleoseismological investigations document at least three deformation events during the very Late
28 Pleistocene (<20 ka) and Holocene. The clue to surface-rupturing episodes, together with the fault
29 dimension inferred by geological mapping and microseismicity distribution, suggest a seismogenic
30 potential of M6.3. Our study provides the second documentation of a major active fault in southern
31 Italy that, as the Irpinia Fault, does not bound a large intermontane basin, but it is nested within the
32 mountain range, weakly modifying the landscape. This demonstrates that standard
33 geomorphological approaches are insufficient to define a proper framework of active faults in this
34 region. More in general, our applications have wide methodological implications for shallow
35 imaging in complex terrains because they clearly illustrate the benefits of combining electrical
36 resistivity and seismic techniques. The proposed multidisciplinary methodology can be effective in
37 regions characterized by young and/or slow slipping active faults.

38

39 Index term: 8109, 8010, 9123,0900, 7221.

40 Keywords: active fault, integrated geophysical investigations, morpho-tectonic analysis,
41 paleoseismology.

42

43 1. Introduction

44

45 Southern Italy is one of the areas with the highest seismic hazard in the Mediterranean region
46 (Fig. 1a). The most large earthquakes ($6.5 \leq M \leq 7$) clustered along the axis of the Apennine range
47 (Fig.1b; CPTI Working Group, 2004), where prevailing normal faulting events are coherent with a
48 NE-oriented extensional regime (Montone et al., 2004). Extensional deformation has been active
49 since Middle Pleistocene (Hippolyte et al., 1994), when it replaced contractional tectonics
50 responsible for the accretion of the Southern Apennines fold-and-thrust belt (Patacca et al., 1990).

51 Active faults identification and characterization present significant challenges in the Southern
52 Apennines. Due to the very recent change in tectonic regime and low extension rates (2-5 mm/yr,

53 Serpelloni et al., 2005), the mountain landscape is still dominated by the inherited structural setting
54 related to contractional tectonics (Pantosti and Valensise, 1990). Consequently, reading the
55 signature of the presently active extensional structures is not straightforward.

56 Besides this difficulty, unfavorable conditions to the preservation of short-term tectonic
57 indicators of faulting (e.g. fault scarps) hamper the identification of major seismogenic faults
58 through geomorphic and structural surface observations. Paleoseismic studies indicate that
59 extensional structures responsible for surface faulting earthquakes (M_w between 6.3 and 7.0) share
60 long recurrence intervals and low slip rates (~ 2 ka and ≤ 1 mm/yr, respectively; see Galli et al.,
61 2008). This faulting behavior coexists to intense erosion/weathering processes caused by a
62 temperate climate, widespread anthropogenic activity. Furthermore, highly erodable terrains are
63 widespread in the mountain belt.

64 The Irpinia Fault, source of the large (M_s 6.9) 1980 southern Italy earthquake (Fig. 1b), well
65 illustrates these difficulties. This fault, recognized by the 1980 co-seismic surface scarp (Westaway
66 and Jackson, 1984; Pantosti and Valensise, 1990), has a negligible cumulative vertical offset (30-50
67 m; Ascione et al., 2003) and does not show clear, long-term morpho-tectonic indicators. Both
68 characteristics are due to a recent fault inception (late Middle Pleistocene; Ascione et al., 2003) and
69 a low slip rate (0.25-0.35 mm/yr; Pantosti et al., 1993). As a result, this major seismogenic fault
70 does not bound a large intermontane basin, as commonly observed in active extensional regions
71 (e.g. Central Nevada Seismic Belt; Wallace, 1984). Rather, it is nested within the mountain range
72 and has not yet produced an evident geomorphic expression.

73 Active fault detection can be further complicated by deep-seated gravitational slope
74 deformations (DGSD), which have been observed along the carbonate mountain slopes of the
75 Apennines, because slope instability often occurs close to Quaternary normal faults (Galadini, 2006,
76 Moro et al., 2009).

77 In such a context, a geological approach based on traditional geomorphic and structural
78 observations is often insufficient for the characterization of active faults (see for a discussion

79 Pantosti and Valensise, 1990). On the contrary, multidisciplinary strategies integrating field studies,
80 paleoseismological investigations and shallow geophysical imaging are required for the definition
81 of a proper framework of active faults (Meghraoui, 2000; Liberty et al., 2003).

82 It is worth here to recall that the last illuminating example of the pitfall of a solely geologic
83 approach for seismic hazard assessment in Italy comes from the 2009, Mw 6.3, normal-faulting
84 earthquake that struck the L'Aquila town in Central Apennines. The earthquake source has been
85 related to a Quaternary fault (Chiarabba et al., 2009), previously recognized through geomorphic
86 observations (Bagnaia et al., 2002), but with poorly constrained geometry, lateral continuity and
87 doubtful seismogenic role (Boncio et al., 2004).

88 In this paper, we present a multidisciplinary study of a Quaternary normal fault in the Val
89 d'Agri area, one of the regions in Italy with the highest seismogenic potential (Fig. 1b). We have
90 targeted the Monte Aquila Fault (MAF) traced along the Monti della Maddalena ridge by Maschio
91 et al. (2005) by morpho-tectonic investigations (Fig. 2). The MAF is only locally recognizable in
92 the field in correspondence of scattered, poorly expressed fault scarps and smoothed warps and its
93 subsurface geometry is unknown. Furthermore, recent activity was only inferred by Maschio et al.
94 (2005) based on the deformation of near-surface colluvia of uncertain age. Nevertheless, the MAF
95 has recently received new attention after a passive seismic survey documenting an intense
96 seismicity related to this structure (Fig. 2; Valoroso et al., 2009).

97 In order to properly characterize this fault, we have developed a multidisciplinary and scale-
98 based investigation strategy consisting of three sequential steps. Detailed geomorphic and structural
99 analyses have been followed by an integrated geophysical investigation, including electrical
100 resistivity tomography (ERT), seismic tomography, seismic reflection imaging and laboratory
101 physical logging of cored sediments. Shallow geophysical imaging has been propaedeutic and
102 complementary to paleoseismological analyses.

103 The integration of advanced geophysical tools plays a primary role in our strategy. Even if
104 high-resolution (HR) seismic reflection imaging and ERT have been extensively used for shallow

105 imaging of active faults in the last decade, the joint application of these techniques is very rare
106 (Wise et al., 2003; Ahmad et al., 2009, McCalpin, 2009). In particular, our joint application of
107 multi-scale seismic tomography and ERT, and the use of laboratory physical logging of cores to
108 detect shallow faulting in recent continental sediments are methodologically innovative. Main
109 specific targets of the geophysical imaging are: (1) the precise position and geometry of the fault,
110 (2) the definition of complementary, multi-scale images of the fault zone, (3) the estimation of fault
111 throw, (4) the recognition of possible structures diagnostic of coseismic surface-faulting (e.g.
112 colluvial packages, Mattson, 2004).

113 As this paper will show, our study illustrates the benefits of using a multidisciplinary approach
114 for shallow fault imaging in complex environments and supplies new information for a better
115 understanding of the MAF.

116

117 2. Tectonic and Seismological Setting

118

119 The Southern Apennines fold-and-thrust belt accreted from Miocene to Early Pleistocene in the
120 westward-directed subduction of the Adriatic-Ionian lithosphere slab (Malinverno and Ryan, 1986;
121 Patacca et al. 1990). Since Middle Pleistocene (500-700 ka; Hippolyte et al., 1994), NE-SW
122 extension together with regional uplift has affected the axial sector of the Apennines, leading to the
123 opening of intermontane basins along NW-striking high-angle normal and oblique faults (Cinque et
124 al., 1993; Hippolyte et al. 1994). However, disruption of pre-Quaternary contractional structures is
125 limited since they still shape the mountain landscape. Seismicity and all stress indicators indicate
126 that the extensional stress regime is ongoing (Fig. 1b; Pondrelli et al., 2006; Montone et al., 2004).

127 The Val d'Agri region hosts one of the largest intermontane basins of the Apennines (Figs. 1
128 and 2). The basin is filled by a continental succession up to 500 m thick, which rests unconformable
129 above the pre-Quaternary bedrock (Mazzoli et al., 2001; Fig. 2). It includes Lower-Upper
130 Pleistocene talus breccia, lacustrine and alluvial deposits (Zembo et al., 2009).

131 An eastern range-bounding fault system controlled the basin opening and long-term evolution
132 since Lower Pleistocene as documented by structural (Cello et al., 2000) and industry reflection
133 profiles (Barchi et al., 2007). The ~30 km long, NW-trending and SW-dipping fault array (Eastern
134 Agri Fault System, EAFS; Fig. 2) is composed of sub-parallel strands with evident long-term
135 geomorphic signatures, and has an integrated vertical displacement of ~500 m (Cello et al., 2003).
136 Fault kinematics analysis documents a main left oblique-slip, but superposition of a second set of
137 slip lineations indicating dip-slip motion is observed on some fault surfaces and is attributed to the
138 Late Pleistocene (Maschio et al., 2005). Based on morphological maturity, large throw and control
139 on basin growth, the EAFS is considered the main seismogenic structure in the region (Michetti et
140 al., 2000; Cello et al., 2000; Cello et al., 2003; Barchi et al., 2007). In this view, no significant
141 active faults are located to the west of the basin (Cello et al., 2003; Barchi et al., 2007). Benedetti et
142 al. (1998) directly related the eastern fault system to the source of a large (M~7) historical
143 earthquake that struck the region in 1857 (Figs. 1 and 2). However, Bucci et al. (2007) and Bucci
144 (2009) have recently questioned the recognition of a presumed coseismic scarp along the EAFS.

145 In an alternative interpretation, Maschio et al. (2005) proposed that since Late Pleistocene
146 extensional deformation has occurred to the SW of the basin along the Monti della Maddalena Fault
147 System (MMFS in Fig. 2). The ~30 km long fault array is composed of two NW-striking, NE-
148 dipping, fault branches aligned with small basins perched at high elevation along the western ridge
149 (Fig. 2). Like the Irpinia Fault, the MMFS does not show evident long-term geomorphic features
150 and is mostly expressed at the surface by small, often poorly preserved scarps and warps. Fault
151 lineation analysis indicates dip-slip motion with a ~NE average extensional slip vector.

152 The importance of normal faulting along the Monti della Maddalena ridge since the latest
153 Middle Pleistocene has been recently supported by Zembo et al., (2009) based on a detailed
154 stratigraphic reconstruction of the basin infill. The shift of active extensional faulting from the
155 northeastern to the southwestern margin of the basin is also suggested by a depocenter imaged
156 beneath the western portion of the basin by deep electrical tomography (Colella et al., 2004). Based

157 on a detailed examination of felt reports, Burrato and Valensise (2008) proposed that the MMFS
158 ruptured during the 1857 earthquake.

159 Despite of a high seismogenic potential, the Val d'Agri appears as a region of very low seismic
160 release in the instrumental catalogues (Cucci et al., 2004). Present-day seismicity was investigated
161 in detail by Valoroso et al. (2009) during 2005-2006 by a very dense passive seismic survey. A
162 major cluster of almost 2000 low-magnitude earthquakes ($M_L < 3$), occurring in the 1-6 km depth
163 range, was localized to the SW of the basin (Fig. 2). Conversely, only a few, sparse events were
164 localized beneath the basin and the eastern ridge. The cluster shows prevailing NW-trending
165 normal-faulting mechanisms and is spatially correlated with the southern termination of the MMFS
166 (Valoroso et al., 2009). In particular, around 70 earthquakes accurately located by 3D Local
167 Earthquake Tomography (hypocentral errors < 200 m; Valoroso et al., 2008) fall inside a NW-
168 trending region to the NE of the trace of the MAF (Fig. 3a). Projection of the hypocenters along a
169 SW-NE striking section reveals a clear alignment of events along a NE-dipping ($\sim 50^\circ$) straight
170 plane that extends NW-SE along the eastern slope of the Monti della Maddalena ridge from 1 to 6.5
171 km depth (Fig. 3b). Accurate focal solutions consistently display NW-striking extensional
172 mechanisms for this seismically inferred fault. Remarkably, the surface projection of this fault
173 matches the MAF (Valoroso et al., 2009): the plane emerges a few hundreds of meters to the SW of
174 the fault trace (Fig. 3b), compatible with the slightly higher ($\sim 60^\circ$) fault dip mapped at the surface
175 (Fig. 4).

176 Therefore, the new earthquake data of Valoroso et al. (2009) corroborate active extension along
177 the Monti della Maddalena ridge. This result is consistent with a significant crustal seismic
178 anisotropy revealed by S-wave splitting analysis (Pastori et al., 2009). Furthermore, the fact that the
179 seismically active crustal fault identified by Valoroso et al. (2009) is geometrically and
180 kinematically compatible with the MAF agrees with a tectonic origin of this structure rather than
181 with a DGSD.

182

3. Morphological-tectonic analysis of the Monte Aquila Fault

The NE-dipping MAF is a ~18 km long strand within the southern branch of the MMFS and consists of three en-echelon right-stepping segments (Fig. 2). The fault cuts across Mesozoic slope-facies limestones thrust above Lagonegro basin rocks (Fig. 2), with the thrust contact marked by a huge cataclasite carbonate belt. The fault trace is underlined by small intermontane basins filled by recent alluvial and colluvial deposits, which locally rest above Quaternary matrix-supported carbonate breccias (Macchitelle, La Gattina and Petenella basins in Fig. 4).

Our investigations focused on the southern half stretch of the ~10 km long northern segment (Fig. 4), where the fault shows the best-preserved geomorphic signatures. The fault is expressed both by bedrock slip surfaces and by scarps/warps in Late Pleistocene-Holocene colluvium (Fig. 4).

Individual scarplets follow an alignment that turns from NW-SE to WNW-ESE, moving from south to north, and are arranged in a right-stepping en-echelon fashion, similar to the large-scale segmentation pattern (Figs. 2 and 4). Locally, two or more sub-parallel scarps or fault zones (m-scale shear zones made of closely-spaced faults) have been observed both in bedrock and in recent deposits. Minor-length antithetic faults are locally present (Fig. 4).

The dip of bedrock fault planes observed in surface exposures or in paleoseismological trenches typically ranges from 60° to 80° for dip-slip and oblique slip faults, respectively. Inversion of slip lineations collected on the ~290° striking fault at Cava site yields a normal pseudo-focal mechanism with a NE-SW extension axis (Fig. 4). Similarly, slip lineations collected on the fault exposed in trench, although yielding a transtensional mechanism, are consistent with an extension axis trending N19°E (Trincea site in Fig. 4). Indeed, the moderate dextral strike-slip component of this mechanism can be related to a local E-W bend of the fault (Figs. 4 and 5a).

The MAF is well recognizable in the ~1.5 km long and up to 0.5 km wide Macchitelle basin (Fig. 5a). The basin is bounded by Mesozoic limestone of the Monte Aquila peak to the NE and by Cretaceous shale and argillite with thin limestone intercalations of the Lagonegro basin to the SW

(Fig. 5b). At this site, seven scarplets and warps have been recognized (Fig. 5a). Four high-precision topographic profiles show that the slope angle and height of individual scarps change moving along strike and clearly depend on the near-surface lithology (Figs. 5a, 6 and 7). At Scarpata site, where limestone are nearly outcropping, a steep ($\sim 60^\circ$) scarp can be laterally followed for several meters. The scarp is 4.3 m high and a surface offset of 3.3 m has been estimated using parallel surface assumption (Fig. 6a). Moving to the SE, across more erodable terrains of the Lagonegro basin and recent deposits, the scarp is subdued and marked by surface warps. At Trincea site, where the fault juxtaposes weathered shale against colluvium, the scarp is 4 m high, has a gentler slope, and the surface offset is 2 m (Fig. 6b). At Covoni site, a 120 m long profile exhibits a dominant large-wavelength concave shape, with a small-wavelength convex pattern superposed between 50 and 80 m (Fig. 6c). We interpreted this warp as the geomorphic mark of the fault across colluvium and alluvia. Unfortunately, reworking caused by a country road prevents the proper reconstruction of the scarp between 50 and 60 m, where we infer the main fault is located. Nevertheless, the analysis of the 60-80 m sub-section reveals a secondary 2.1 m high scarp, with a surface offset of 1.7 m (Fig. 6c). Similarly, at Fornace site the MAF is traced within colluvium following a long-wavelength (~ 60 m) warp (Fig. 7). This warp is 3.5 m high and the estimated surface offset is 2.1 m.

A rough estimate of the MAF total throw is provided by displacement of geologic and geomorphologic markers. To the SE of Fornace site, a low-angle thrust shows ~ 50 m vertical offset (Fig. 5a). Substantial uncertainty on this estimate arises from the fact that thrusts in the region were refolded during Neogene (Mazzoli et al., 2001; Ferranti et al., 2005). Relics of a Middle Pleistocene erosional surface of probable fluvial origin (Boenzi et al., 2004) suggest a comparable displacement (Figs. 5a-b).

232

233 4. HR multi-scale imaging of the Monte Aquila Fault

234

235 The MAF has been investigated along three SW-trending profiles in the Macchitelle basin
 236 (Figure 5a). HR seismic tomography, reflection profiling and ERT have been jointly used at Trincea
 237 and Fornace sites. Seismic profiling was instead impractical at Covoni site due to a thick vegetation
 238 cover. ERT and seismic tomography follow a multi-scale exploration strategy. Collocated electrical
 239 resistivity and seismic tomography first provide complementary images of the basin structure down
 240 to 50-70 m depth, and subsequently target the near-surface structure of the fault zone ($< 10\text{-}15$ m
 241 depth) with improved spatial resolution. Data acquisition parameters are reported in Table 1.

242

243 **4.1 Electrical Resistivity Tomography**

244 Shallow faults have become a frequent target of ERT in the last decade (e.g. Suzuki et al., 2000;
 245 Caputo et al., 2003; Wise et al., 2003; Nguyen et al., 2005). We carried out ERT by using different
 246 array configurations (Wenner-Schlumberger and Dipole-Dipole) and electrode spacing to obtain
 247 resistivity images with different investigation depths and spatial resolution (Table 1). Apparent
 248 resistivity data were inverted by the RES2DINV software (Loke, 2001).

249 In the Trincea site, the profile runs above slope-facies Mesozoic limestone, shale of the
 250 Lagonegro basin and recent deposits (Fig. 5a). The fault scarp is crossed at ~ 90 m. The resistivity
 251 pattern is very complex (Fig. 8a). While high resistivity values ($\rho > 250 \Omega \text{ m}$) can be related to
 252 limestone (Units 4 and 4?), relatively low resistivity values ($\rho < 70 \Omega \text{ m}$) might be attributed either
 253 to shale bedrock or to shallow sediments. This ambiguity prevents the interpretation of two low-
 254 resistivity bodies ($\rho < 70 \Omega \text{ m}$), with values as small as $15 \Omega \text{ m}$, imaged at 45-90 m and 115–210 m.
 255 Based on seismic and trench data, the SW body can be related to the shale, weathered bedrock (Unit
 256 5), partially covered by carbonate coarse debris (Unit 3), whereas the NE one corresponds to recent
 257 sediments (Unit 2) overlying the high-resistivity carbonate bedrock. The body with moderate
 258 resistivity values (from 70 to $150 \Omega \text{ m}$; Unit Un), in between these two conductive regions, might
 259 be attributed either to shale bedrock or to recent sediments. This locally prevents the imaging of the
 260 substratum, and, more importantly, the fault detection. Seismic profiling and later trenching (picture

261 inset in Fig. 8a) have proved that the fault zone corresponds to the weak lateral variation of
262 resistivity between 90 and 100 m.

263

264 In the Covoni site (Fig. 5a), we carried out a HR and a very high-resolution (VHR) tomography
265 (Table 1). The HR survey crosses the main fault zone inferred from field observations at ~65 m and
266 the secondary fault scarp at ~80 m (Fig. 6c). A broad high-resistivity region between 30-65 m, with
267 values exceeding 250 Ω m, is interpreted as the limestone bedrock (Unit 3; Fig. 9b). Low-resistivity
268 materials ($\rho < 40$ Ω m, Unit 4), bounding this region to the SW, are related to exposed argillite of
269 the Lagonegro basin (Fig. 5a). The limestone bedrock abruptly deepens at ~65 m, and a conductive
270 asymmetric wedge ($\rho < 70$ Ω m) concurrently develops in the block to the NE of the fault. The
271 wedge, which gently thickens towards SW reaching about 20 m depth, exhibits values as low as 15
272 Ω m related to recent deposits mainly consisting of saturated alluvia (Unit 2). The resulting lateral
273 change is very strong (ρ sharply decreases from 250 to 15 Ω m over 10 m distance range) and
274 provides evidence for a NE-dipping fault. Normal-faulting activity is further supported by: (1) a SW
275 dip of the high-resistivity ($\rho > 300$ Ω m) limestone bedrock in the hanging-wall, which suggests
276 back-tilt toward the fault, (2) a near-surface body (Unit 1, $\rho \sim 40$ Ω m) covering Unit 2 just ahead
277 the main fault zone that could indicate a colluvial package.

278 The VHR survey targets the near-surface body (Unit 1). The model shows very conductive ($\rho \sim$
279 15-40 Ω m) deposits, 4 m thick at least, adjacent to the main fault zone (Fig. 9a). A low-resistivity
280 wedge, growing near an ancillary fault splay at ~78 m, has been confirmed by trench data (see inset
281 picture in Fig. 9a).

282

283 The Fornace site has been investigated by two collocated ERTs (Table 1). The HR survey (Fig.
284 10b) entirely runs above colluvial and alluvial deposits, intercepting the surface warping between
285 80-150 m (Fig. 7). Resistivity images at Fornace and Covoni sites are comparable (Figs. 9b and

10b). To the SW, a relatively high-resistivity body ($\rho > 160 \Omega \text{ m}$) defines a shallow substratum (Unit 3), which is covered by a thin conductive layer ($\rho < 40 \Omega \text{ m}$) of colluvial soils (Fig. 10b). Below the surface warping, the substratum deepens to $\sim 20 \text{ m}$ under conductive deposits. Further to the NE, the low-resistivity layer is laterally homogenous (Unit 2) and covers the high-resistivity limestone bedrock ($\rho > 250 \Omega \text{ m}$) that gently dips SW between 160 and 220 m (Fig. 10b). The very-low resistivity values of Unit 2, as small as $5\text{-}10 \Omega \text{ m}$, are indicative of saturated loose alluvia, consistently with a near-surface water table observed during the survey.

The VHR ERT (Fig. 10a) was specifically designed to detect shallow colluvial wedges, possibly related to surface rupturing episodes, in correspondence of the surface warping. The model reveals a low-resistivity body developed above the rapidly deepening bedrock. Between 124 and 172 m, this package consists of a very conductive unit ($15\text{-}25 \Omega \text{ m}$, Unit 1b) and of a shallower asymmetric, 4-6 m thick wedge ($\sim 40 \Omega \text{ m}$, Unit 1a).

Although the lateral resistivity variations at Fornace site are smoother than at Covoni, model features suggest a normal fault below the suspected warping.

300

301 **4.2 Seismic Imaging**

Our exploration strategy combines shallow reflection imaging (e.g. Miller et al., 1990) and traveltimes tomography (e.g. Morey and Schuster, 1999). We jointly collected small-offset, near-vertical reflection data and dense wide-aperture data in both sites (Table 1, Fig. S1 in the auxiliary material). While reflection profiling aims at producing a stack section across the fault zone by standard Common-Depth-Point (CDP) processing (Steeple and Miller, 1998), dense wide-aperture profiling aims at imaging the basin and the shallow structure of the fault by multi-scale tomography. We used a non-linear tomographic algorithm specifically designed for the multi-scale imaging of crustal structures with strong lateral V_p variations (Improta et al., 2002; Improta and Corciulo, 2006) and successfully adapted to shallow targets (Improta et al., 2003). A succession of inversions is run by progressively reducing the spacing of the velocity grid (i.e. increasing the spatial

312 resolution), and for each run the best fit model is found by a combined global/local exploration of
313 the model space without using *a priori* information (details on the survey and tomographic
314 inversion are available in the auxiliary material).

315 In the Trincea site, the dense wide-aperture profile overlaps the ERT between 50 and 228 m
316 (Fig. 8a-b). Around 4550 first-arrival traveltimes hand picked with an average error of 3 ms were
317 input to the tomography. We discuss model features for a long- and short-wavelength models (Fig.
318 8b and Fig. 8c, respectively). The first model, obtained at the 6th run of the multi-scale inversion, is
319 resolved down to 40-50 m depth and illuminates the whole basin with the best compromise between
320 spatial resolution and resolution depth (Fig. S2a). The short-wavelength model results from the 13th
321 (final) inversion run. It resolves the small-scale structure, but only above 10-15 m depth (Fig. S2b).

322 The long-wavelength model exhibits a complex pattern of high-Vp zones (HVZ) (2500-3500
323 m/s), which can be reasonably associated to the basin substratum (Fig. 7b). Two shallow HVZs
324 characterize both model sides. On the SW side, velocity increases quite sharply from 400 m/s to
325 3000 m/s over a 10 m depth range, in agreement with the nearly-outcropping argillite bedrock.
326 Below the surface scarp, the HVZ is interrupted by a strong lateral variation revealed by an abrupt
327 deepening of the 2250-3000 m/s contours showing ~30 m of vertical separation. These contours,
328 which gently dip SW between 50 and 90 m, define a major step in the bedrock. Concurrently, low-
329 Vp shallow deposits rapidly thicken above the down-thrown block. These traits are indicative of a
330 normal fault juxtaposing bedrock against recent sediments. The high-velocity substratum gently
331 deepens between 100 and 140 m under a broad low-Vp region (LVZ), which extends down to ~30
332 m depth with value around 1500 m/s. The HVZ rises at the NE end of the profile.

333 The shallow short-wavelength model (Fig. 8c) outlines the rapid thickening of soft deposits to
334 the NE of the fault scarp. A low-Vp shallow layer ($400 < V_p < 1000$ m/s) thickens between 95 and
335 140 m reaching a maximum depth of 11-14 below the surface. The 1000 m/s contour delineates a
336 wedge-like body, whose southern vertex lies on a deeper small-scale step (see the 1250-2000 m/s
337 contours at ~100 m distance in Fig. 8c). The presence of two low-velocity colluvial packages (see

338 Mattson, 2004) within this wedge is inferred from sags in the contours. A shallow package, 6-9 m
339 thick, is clearly delineated by the sag in the 700-800 m/s contours positioned between 107 and 116
340 m at ~6 m below the ground level (Fig. 8c and body “a” in Fig. S3a). A deeper package (~10 m
341 below ground level), with a comparable thickness, may be related to the sag in the 900-1100 m/s
342 contours positioned at ~124 m (Fig. 8c and body “b” in Fig. S3a). As for other seismically imaged
343 colluvial packages reported in literature (Morey and Schuster, 1999; Sheley et al., 2003; Mattson,
344 2004), seismic ray density plots back packages detection. In fact, ray paths tend to skirt both the
345 low-velocity regions and preferentially pass through the surrounding higher velocity regions (Fig.
346 S3b).

347 The reflection profile shows evident reflection truncations between 90 and 105 m, which reveal
348 at least three NE-dipping fault splays (“f₁₋₃” in Fig. 11a). These splays are located in correspondence
349 of the strong lateral change in the large-wavelength tomogram (Fig. 8b) and cause a rapid
350 deepening of the basin substratum down to 90 ms TWT. To the NE of this fault zone, the sediment-
351 substratum unconformity can be related to a deeper reflector (event “b” between 110-130 ms TWT
352 in Fig. 11a), which gently dips NE and appears further displaced by a synthetic fault at ~125 m (“f₄”
353 in Fig. 11a) and by an antithetic fault at ~145 m. On the NE side of the profile, prominent and
354 continuous reflectors located at ~100 ms between 170 and 200 m suggests a rapid rise of the
355 substratum (event “c”). A NE-dipping discontinuity inside the substratum is suggested by some
356 events alignments around 100-140 ms (event “t”). Reflectivity of the shallow section strongly varies
357 along the profile (Fig. 11a). To the SW, strong continuous events can be related to Lagonegro
358 bedded shale and argillite. A wedge-like reflectivity zone between 105 and 120 m (region “cp” in
359 Fig. 11a) spatially correlates with the shallower colluvial package inferred by tomography (Figs
360 12c-b and Fig. S3). In the central part of the basin, a low-reflectivity region between “f₄” and “c”
361 (Fig. 11a) corresponds to the alluvial and colluvial infill. Finally, on the NE end of the profile,
362 strong but discontinuous events above reflector “c” might indicate a coarser infill (carbonate debris
363 breccias) resting upon the bedded substratum.

364

365 In the Fornace site, the dense wide-aperture profile overlaps the ERT between 25 and 235 m
366 (Fig. 10b and Fig. 10c). We inverted around 3700 first-arrival readings with an average picking
367 error of 4 ms. Figures 10c and 10d show a long-wavelength and short-wavelength models,
368 characterized by a resolution depth of 40 and 20 m, respectively (Fig. S4). The first model shows a
369 HVZ in the lower part, with values exceeding 3000 m/s, corresponding to the bedrock. The HVZ is
370 deeper on the NE side (160-230 m) and shallower in the central part (80-130 m), where velocity
371 increases quite rapidly from 400 m/s to 2500 m/s at 10 m depth. A NE deepening of the 2500-3000
372 m/s contours around 140 m distance reveals the resulting lateral velocity variation. Although this
373 trait is weaker than the strong lateral variation imaged below the scarp at Trincea site (Fig. 8b), it
374 suggests a step within the substratum below the surface warping.

375 In the short-wavelength model (Fig. 10d) an almost homogenous layer ($V_p \sim 1600$ m/s)
376 develops above the NE bedrock block, reaching a thickness of 15-18 m. This layer laterally grades
377 into a low-velocity asymmetric wedge outlined by a sag in the 1000-1400 m/s contours. This wedge
378 is located just to the NE of the surface warping, gently dips to SW and is ~9 m thick. As a whole,
379 this velocity structure resembles the resistivity patterns (Figs. 10a-b) and is compatible with normal
380 faulting below the suspected surface warping.

381 This interpretation is consistent with the reflection profile (Fig. 11b). In spite of a low quality, it
382 shows deep reflection truncations (“A”) around 125 m between 180-260 ms TWT, accompanied
383 upwards to warped events (“B” and “S” between 40-80 ms TWT). Both features are compatible
384 with a NE-dipping normal fault, whose surface projection matches the surface warping.

385

386

387 5. Paleoseismology along the Monte Aquila Fault

388

389 5.1. Trench Investigations

390 In order to directly investigate and characterize the MAF, we opened two trenches at Trincea
391 and Covoni sites across two differently oriented sections of the scarp ~200 m apart (Fig. 5a). In the
392 Trincea site, the trench is perpendicular to a WNW-ESE bend of the NW-trending scarp that
393 juxtaposes bedrock against colluvia (inset in Fig. 8a). We used geophysical imaging to optimize
394 trench location: the excavation is tied to the fault scarp (Fig. 6b) and extends to the NE above the
395 seismically imaged colluvial packages (Fig. 12b) and easternmost fault splay (“f₄” in Fig. 12c).

396 The trench exposed a sequence of predominantly fine colluvial and slope deposits (mainly silt
397 and clay), with diffuse fine-sized sub-angular clasts mainly of calcareous mudstone (Fig. 13).
398 Sparse manganese nodules and reworked/weathered pumices are quite common. Two paleosols
399 (Units C and E) and two weathered volcanic layers (Units P and Q) were found in the central-
400 southern and central section, respectively.

401 Four charcoal samples were dated by AMS from Units R, T, F, E, giving ages ranging from 7.5
402 to 20.6 ka B.C. (samples AQ-S1, AQ-S2, AQ-S3, AQ-S4, see Table 2 and Fig. 13). These units are
403 considerably younger with respect to tephra Unit Q, including pumices, which was dated at 266 ± 5
404 kyr in a previous tephrochronological study ($^{40}\text{Ar}/^{39}\text{Ar}$ dating, D’Addezio et al., 2006). Taking into
405 account the stratigraphic position of Unit Q, exposed at 2.0-2.5 m depth inside a massive reddish
406 clay slope wash deposit, together with the absence of a clear erosional surface above it, it is difficult
407 to reconcile the Middle Pleistocene age of this pumice layer with the ^{14}C ages of the upper units. In
408 our opinion, the interpretation of Unit Q as a reworked horizon represents a plausible solution,
409 because the primary deposition of Unit Q from a pyroclastic fall-out is not certain (D’Addezio et al.,
410 2006)

411 Three main deformation zones were identified in the trench. In the 12 m-wide fault zone 1,
412 deformation is expressed by a main fault plane juxtaposing the bedrock (weathered shale) against
413 colluvia, and by a series of high-angle synthetic and antithetic normal faults, which define a graben-
414 like structure. In fault zone 2 units are displaced northward along low-angle reverse faults. Fault
415 zone 3 is composed of a main high-angle normal fault plus three synthetic structures.

416 We recognized at least three single events of deformation. Event 1 affects the sequence up to
417 Unit C (see upper fault terminations in fault zone 1). The top of this unit is considered as event 1
418 horizon and the colluvial wedge Unit B is interpreted as the post event deposit. We suspect that Unit
419 C was continuous all along the trench at the time of this event and probably deformation took place
420 also along the main fault plane. Although with uncertainties, we tentatively estimate a minimum
421 vertical slip of 40-70 cm by considering both the vertical separation of the event horizon across
422 fault zone 1 (assuming a dip similar to the present surface) and the thickness of the colluvial wedge
423 (Unit B). Evidence for event 2 appears distributed along the whole section. In fault zone 1, the
424 lower units, up to Unit I, present nearly twice the offset with respect to the overlying deposits (see
425 also upper fault termination at meter 12), while in fault zone 2 many fault terminations occur at the
426 top of Unit I. Within fault zone 3, the deformation observed along the main fault plane at meter 38
427 could be interpreted either as produced during event 2 or during an older event, as indicated by
428 structural and stratigraphic relations. Hence, the event 2 horizon can be located at the top of Unit I
429 or alternatively within the lower part of Unit G, which would correspond to the post event deposit
430 filling the space created by event 2 (Fig. 13).

431 Discrimination of event 3 relies on the upper fault terminations sealed by the upper part of Unit
432 O visible in fault zone 3. Event 3 is also inferred by the fact that Unit Q is affected by a larger
433 vertical displacement with respect to the units above along a fault plane at meter 19. Minimum slip
434 per event 3 can be inferred from the retro-deformation of previous events along the fault at meter
435 19, resulting in a vertical separation of about 30-40 cm for Unit Q. The event 3 horizon should be
436 placed on top of Unit Q or alternatively within the upper part of Unit O.

437 Despite of a well readable stratigraphy, the three deformation events cannot be dated. Samples
438 AQ-S1, AQ-S3, and AQ-S4, coming from different stratigraphic position, share comparable ages
439 and 13C/12C ratio (Table 2). This likely points to a single parent material that yielded the retrieved
440 ages. Moreover, samples AQ-S1 and AQ-S2 show a time reversal with respect to their stratigraphic
441 relationship. Due to these difficulties, paleoseismological analyses can exclusively indicate that

442 three events occurred in the latest Pleistocene and possibly in the Holocene.

443

444 Unfavorable logistic conditions hindered trench excavation in the Covoni site. We opened a NE-
445 striking, 12 m long trench located only in the hanging-wall of the main fault detected by the HR
446 ERT (Fig. 9b). Nevertheless, the trench cross cut the secondary fault imaged ~15 m to the NE of the
447 main fault-zone by the VHR ERT (Fig. 9a).

448 The trench exposed predominantly fine sediments (silt and clay), with intercalated small lenses
449 of mainly pebble-sized sub-angular clasts (Fig. 14). Sparse manganese nodules,
450 reworked/weathered pumices and calcareous concretions are common. A paleosol (Unit C1) and
451 well developed colluvium units (Units N and N1) were recognized in the south-western and north-
452 eastern section of the trench, respectively. Three charcoal samples were dated by AMS from Units
453 B, C1 and D (samples COV-7, COV-1, COV-13 respectively, see Table 2 and Fig. 14). They
454 yielded ages ranging from 800 B.C. to 1400 A.D..

455 The trench shows one deformation zone characterized by an abrupt, sub-vertical contact at
456 meter 8 (Fig. 14). Stratigraphic and structural analyses allowed us to interpret this contact as a NE-
457 dipping, fault plane with a mainly dip-slip motion. The whole deformation zone is marked by
458 important water circulation with precipitation of calcium carbonate at several patches (Unit T). This
459 hampers the discrimination of different deformational events, as well as the estimation of slip
460 amount for single events. Deformation appears to involve the whole section up to Unit C. We
461 interpret Unit N as a colluvial wedge derived from the erosion of Unit C, with some remnants of C
462 (Unit C1?) found also at the base of Unit N in the fault hanging-wall. The event horizon can be
463 placed at the top of Unit C, in the footwall, and at the base of Unit N, in the hanging-wall (top of
464 Unit C1?). The fault zone is clearly sealed by Unit B, interpreted as a post-event deposit that covers
465 the colluvial wedge (Unit N). An erosional surface separates Unit B from active soils (Unit A2) in
466 the northeastern section of the trench, where it cuts across an agriculture field subjected to intense
467 ploughing. The erosion of colluvial Unit B allows explaining its anomalous thinning in fault

468 hangingwall.

469 The stratigraphic position of the event horizon and the dated samples (Fig. 14 and Table 2)
470 suggest that a deformation event occurred between 510 B.C. and 1400 A.D., with the older part of
471 the interval preferred because of the proximity of sample COV-1 to the event horizon. Although
472 with uncertainty, we infer a vertical slip of 50-70 cm for this event by considering the thickness of
473 the colluvial wedges (Units N and N1) and the separation of the event horizon across the fault zone.

474

475 **5.2. HR physical logging of cored sediments**

476 As trenching was not permitted at the site Fornace, we used coring as an alternative tool to
477 directly investigate the surface warping. Cores were extracted from 8 boreholes drilled by a
478 vibracoring (gasoline power percussion hammer) down to 7 m depth (Fig. 7). Boreholes FC-03, FC-
479 05/06, FC-07/08 specifically targeted the fault zone detected by ERT (Fig. 10a).

480 Boreholes penetrated a sequence of fine sediments with sparse, weathered pumices and thin
481 gravelly lenses. The sequence mainly consists of decimetric layers with gradual contacts, which
482 were grouped based on sedimentary and stratigraphic characteristics (Fig. 7). *Unit A* is the active
483 clayey soil (20-40 cm thick). *Unit B* includes a brown-reddish clayey silt with pumices occasionally
484 organized as thin layers, some blackish green alterations (mainly manganese) and rare lenses of
485 gravel in silty-clay matrix. *Unit B* shows a gradual transition to *Unit C* that is characterized by a
486 finer matrix (silty-clay to clay) and sparser pumices and alterations. *Unit Bd* is a cemented
487 carbonate breccia, derived from the alteration of the limestone bedrock. Only FC-01, FC-05 and
488 FC-07 reached *Unit Bd*. Both FC-01 and FC-05, located 27 m apart in the presumed footwall,
489 encountered the bedrock at 5 m depth, mimicking the topographic gradient (Fig. 7). Conversely,
490 FC-07 documents an abrupt NE deepening of 1.8 m of the bedrock with respect to FC-05 that is
491 only 5 m apart. This deepening is in good agreement with the VHR ERT (Fig. 10a).

492 Although the bedrock step between FC-05 and FC-07 and the concurrent NE thickening of Unit
493 B support the presence of a fault zone (Fig. 7), stratigraphic analysis does not allow a HR

494 correlation necessary to detect possible deformation events. To achieve this issue, we
495 complemented stratigraphic analysis with laboratory HR measurements of physical properties of
496 cores (Iorio et al., 2004). Laboratory physical logging was performed by a GEOTEK Multi-Sensor
497 Core Logger to measure the following properties: (1) volume magnetic susceptibility, (2) GRAPE
498 (Gamma Ray Attenuation Porosity Evaluator) density, (3) P-wave velocity, and (4) reflectance %.
499 Logging were done at a centimetric scale on the almost undisturbed cores FC-06 and FC-08,
500 sampled down to 4 m depth in correspondence of FC-05 and FC-07, respectively. Thus, FC-06 is
501 located in the footwall and FC-08 in the presumed hanging-wall (Fig. 10a).

502 The magnetic susceptibility logs are highly informative. In fact, due to the presence of
503 significant amount of volcanic materials, both sparse within the layers and occasionally organized
504 in small lenses, evident peaks, troughs and characteristic trends allowed a reliable correlation of FC-
505 06 and FC-08 (Fig. 15). In the following section, we discuss the two magnetic susceptibility logs
506 (the reader can refer to Appendix A for the remaining physical logs and for details on laboratory
507 measurements).

508 Overall, the logs in Figure 15 present a similar trend. The FC-06 log can be summarized as
509 follow: a plateau with an average value (a.v. hereinafter) of $90 \text{ SI} \times 10^{-5}$ (0-0.7 m depth); an abrupt
510 drop down to $5 \text{ SI} \times 10^{-5}$; (0.7-0.9 m); a gradual increase up to $30 \text{ SI} \times 10^{-5}$ (0.9-1.7 m); a rapid
511 increasing trend with overlapped pronounced peaks with values as large as $1000 \text{ SI} \times 10^{-5}$ (1.7-2.5
512 m); a plateau (a.v. $250 \text{ SI} \times 10^{-5}$), with overlapped high frequency peaks and troughs (2.5-3.3 m); a
513 general decreasing trend (from 3.3 m to final depth).

514 Despite of comparable trends, magnetic susceptibility values for FC-06 and FC-08 are
515 significantly different below 2 m depth, where FC-08 presents values ($400\text{-}1500 \text{ SI} \times 10^{-5}$)
516 systematically larger with respect to FC-06 ($300\text{-}400 \text{ SI} \times 10^{-5}$) (Fig. 15 and Fig. S5). This trait,
517 which makes single peaks and troughs less evident on FC-08 log, indicates a significant enrichment
518 in volcanic materials with respect to core FC-06, as expected in the near-fault hanging-wall.

519 We carefully inspected the magnetic susceptibility logs to identify single, prominent peaks and

520 troughs, as well as characteristic features that could be correlated among cores. As result, we
521 recognized 22 homologous points (Fig. 15). These points were subsequently checked on the
522 remaining physical logs to further constrain our interpretation. Ten correlated piercing points were
523 identified in the density log, whereas the correlations for P-wave velocity and total reflectance
524 furnished only 5 and 8 homologous points, respectively (see Fig. S6 and Appendix A).

525 The log correlation proved that FC-08 core lacks the shallower deposits (about 40 cm) likely
526 because of intense ploughing (Fig. 15). Thus, under the assumption that the shallower part of the
527 sequence should have been deposited consistent to the present slope, FC-08 log has been shifted 40
528 cm deeper with respect to FC-06 (Figs. 15 and S6). Remarkably, the HR correlation highlights that
529 magnetic susceptibility homologous points show a clear unsteady downward increment of the
530 corresponding depths on FC-08 with respect to FC-06 (Fig. 15). Thus, for each physical property
531 we measured the vertical offset shown by all the pairs of piercing points and plotted these values vs
532 the depth of FC-08 (Fig. 16). Figure 16 also reports the average value of offset computed for those
533 homologous piercing points that were recognizable in at least three of the four measured physical
534 logs (Figs. 15 and S6).

535 Remarkably, the vertical offset measurements do not align along a straight line, as expected for
536 a constant filling of a depression (Fig. 16). In fact, the offset vs depth curve shows a staircase
537 pattern, outlining three groups of layers with a well-defined offset (A, B, C in Fig. 16), separated by
538 two groups of layers where the offset appears to decrease gradually upwards. Average offsets,
539 calculated for A, B, C groups, suggest null offset from 0 to 60 cm depth, 25 cm offset from 120 to
540 220 cm depth, and 70 cm offset from 280 to 330 cm depth. We interpret this vertical offset
541 distribution as due to two events of displacement able to produce a vertical separation at the surface
542 of about 30-40 cm each.

543

544 6. Discussion

545

546 This study illustrates aim, strategy and advantages of a multidisciplinary and scale-based
547 investigation approach and has wide methodological implications for shallow geophysical imaging.

548 Regional morpho-tectonic investigations on the whole MMFS (Maschio et al., 2005) were
549 pivotal for the recognition of fault strands bearing indications of recent deformation (e.g. the MAF).
550 A detailed geologic field survey along the MAF allowed the mapping of short-term tectonic
551 indicators (scarps and warps) and the identification of favorable sites for target-oriented geophysical
552 investigations. On the one hand, HR geophysical surveying complemented field geologic survey to
553 define the basin structure and to constrain the fault geometry and throw. On the other hand, VHR
554 shallow imaging (< 10-15 m depth) pinpointed the fault zone with an accuracy of few meters, thus
555 giving valuable constraints for later trenching and drilling.

556 Because the shallow architecture of a fault zone can vary greatly, and this impacts the physical
557 parameters distribution, the comparison of resistivity, velocity and reflectivity images, as discussed
558 in the following, is a key ingredient to properly constrain the fault geometry and relate faults
559 recognized in trenches to deep structures.

560

561 **6.1. Geophysical imaging: effectiveness of the multidisciplinary approach**

562 The Trincea site provides an illuminating example of the advantages of the joint application of
563 ERT and seismic methods because ERT alone provides insufficient or even misleading information
564 (Figs. 8a-c and 11a). Below the scarp, the fault juxtaposing bedrock shale against colluvial clays
565 results in a weak lateral resistivity variation that conspires against electrical tomography (Fig. 8a).
566 Noteworthy, the weathered shale bedrock exhibits resistivity values even smaller (10-25 Ω m, Unit
567 5) than the colluvial soils exposed in the trench (40-100 Ω m, Units 1 and Un). Under this
568 circumstance, the fault zone is pinpointed by rapid lateral Vp variations observed both at depth (Fig.
569 8b) and in the very near-surface (Fig. 8c), which correspond to evident reflection truncations in the
570 stack section (Fig. 11a).

571 Nonetheless, comparison between seismic and resistivity images is helpful to distinguish

572 between limestone and shale bedrock, the former highlighted by high resistivity and Vp values, the
573 latter by very-low resistivity and high-Vp values (Figs. 8a-b). For instance, the conductive and
574 high-Vp region at 50-80 m distance is indicative of the shale bedrock (Unit 5) and the strong
575 resistivity decrease at ~40 m of distance marks the thrust superposition of Mesozoic limestone
576 above Lagonegro shale (Figs. 5a-b).

577 Conversely, the joint interpretation of resistivity and Vp images is quite problematic at the NE
578 basin edge. At a first glance, the shallow high-resistivity region ($\rho > 250 \Omega \text{ m}$; Unit 4?) could be
579 reasonably interpreted as the limestone bedrock covered by conductive recent deposits (Fig. 8a).
580 However, this interpretation contrasts with relatively low-Vp (1500-1750 m/s) values found
581 between 150-190 m down to 30 m depth (Fig. 8b). Two alternative scenarios can be proposed to
582 conciliate high-resistivity and low-Vp values. In a first view, the upper part of the resistive Unit (4?)
583 could consist of carbonate debris breccias, which encircle the Monte Aquila peak on the NE margin
584 of the basin. Alternatively, the resistive Unit (4?) could consist of heavily fractured limestone
585 and/or cataclasite, which mark the thrust contact between limestone and Lagonegro basinal rocks
586 (Figs. 5b). We prefer the second interpretation based on three lines of evidence: (1) thick cataclastic
587 belts crop out close to the northern margin of the basin, (2) the presence of a shallow bedrock at the
588 NE side of the basin is inferred by the strong reflectivity zone “c” (Fig. 11a), (3) a NE dipping
589 reflector (“t” in Fig. 11a) located below these strong events could be interpreted as a low-angle
590 fault, which could represent the northern extension of the thrust contact inferred at the southwestern
591 end of the ERT (Figs. 5a-b and 8a).

592

593 Even if resistivity and Vp images show similar pattern at Fornace site (Figs. 10a-d), ERT is
594 crucial for fault detection because it yields a sharper image of the basin. Differently from Trincea
595 site, here the presence of a limestone bedrock covered by or juxtaposed against clay-rich material
596 across the fault zone (see boreholes in Fig. 7) favors ERT performance. This geologic condition
597 leads to resistivity contrasts 5 to 10 times larger than the velocity ones, because the hanging-wall

598 infill mainly consists of saturated alluvia with relatively large (~ 1600 m/s) Vp values (Fig. 10d).

599 Besides, the shallow VHR ERT shows more details comparing to seismic tomography. This is
600 mainly due to the high sensitivity of ERT to the lithology (e.g. clayey vs sandy content) and water
601 content. Nevertheless, comparison between Vp and resistivity images is useful to further constrain
602 the shallow colluvial body deposited in front of the fault (Figs. 10a and 10d).

603 The multidisciplinary exploration approach was also crucial to constrain the minimum
604 cumulative fault throw. We measured an offset of ~ 25 m from the vertical separation of the high-
605 resistivity bedrock at Fornace and Covoni sites (Fig. 9b and Fig. 10b). At Trincea site, the stack
606 section shows ~ 60 ms of vertical separation for the bedrock reflector across the 35-m-wide fault
607 zone (Figs 11a and 12c), which corresponds to ~ 30 m using an average Vp of 1000 m/s for the
608 sediments, as derived by tomography. This value agrees with the height of the bedrock step inferred
609 by the offset of the 2250-3000 m/s contours in the Vp model (Fig. 8b). We believe that the
610 cumulative fault throw provided by geophysical imaging is a refined, more reliable estimate with
611 respect to the one inferred by displacement of geologic markers (~ 50 m), because of the substantial
612 uncertainties on the pre-Quaternary geometry of the thrust and of the difficulties in correlating
613 geologic or geomorphic features.

614 615 **6.2. Comparison of paleoseismological results with geophysical data**

616 Structures revealed by trenching or inferred by drilling (e.g fault zones, colluvial wedges and
617 bedrock offset) can be reasonably related to deeper structures defined by geophysical imaging.

618 In the Trench site, fault zones recognized in the trench (Fig. 12a) well correlate to fault splays
619 in the reflection profile (Fig. 12c). Fault zone 1, juxtaposing bedrock against recent colluvium, can
620 be related to the deformation zone limited by splays f1 and f3 in the stack section. Fault zone 3,
621 including four splays sealed by near-surface deposits, spatially correlates with splay f4 imaged ~ 35
622 m to the NE of the scarp (~ 125 m in Fig. 12c). A good spatial correlation is also observed between
623 trench data and the two seismically imaged colluvial packages. The deeper colluvial package (“b”

in Fig. 12b and Fig. S3a) is positioned just beneath fault zone 3 (Fig. 12a) and spatially correlates to splay f4 responsible for a significant bedrock offset (~20 ms TWT, Fig. 12c). The shallower package (“a” in Fig. 12b and Fig. S3a) is located in front of fault zone 1 (Fig. 12a) and can be related to the activity of f3 (Fig. 12c). It is worth noting that the colluvial wedge exposed in the trench inside fault zone 1 (Unit B in Fig. 12a and Fig. 13) is related to displacement along more southerly located splays, which show evidence for the more recent activity (event 1 in Fig. 13) and could correspond to f1 or f2 in the stack section.

In the Fornace site, coring combined with geophysical prospecting testifies the rapid NE deepening of the faulted bedrock beneath the surface warp and the concurrent thickening of low-resistivity/velocity recent deposits in the down-thrown side (Figs. 10a-b). Inside the wedge of colluvial materials, the vertical juxtaposition of conductive (~40 Ω m, Unit 1a) and very conductive (15-25 Ω m, Unit 1b) materials (Fig. 10a) agrees with distinction of Units B and C in the core logs, the latter being more clayey and less pebbly. ERT also indicates that the vertical displacement of the bedrock (1.8 m) measured between cores FC-05 and FC-07 represents only a small amount of the total displacement (~25 m), which appears distributed along a deformation zone ~30 m wide (Figs. 10a-b).

In the Covoni site, comparison between the trench log (Fig. 14) and the VHR ERT (Fig. 9a) shows that the fault plane exposed at ~8 m in the trench spatially correlates to the rapid thickening of Unit 1a below the trench bottom. The HR ERT, which locates the main fault zone ~15 m to the SW of this feature, clearly indicates that the fault plane at ~8 m represents a secondary splay in the hanging-wall block of the MAF (Fig. 9b). Furthermore, the lack of a signature in the HR ERT model suggests a cumulative vertical slip of a few meters for the secondary splay, below the resolution limit of the survey (~5 m).

6.3. Implications for fault behavior and seismogenic potential

The main result of paleoseismological analyses is the evidence for distinct episodes of

650 displacement during the latest Pleistocene (< 20 ka) and Holocene. This agrees with the detection of
651 low-velocity/low-resistivity colluvial packages buried just in front of the scarp which, following
652 Mattson (2004), can be considered diagnostic of coseismic surface-faulting episodes.

653 The recognized deformation events could be ascribed to a gravitational origin as well, with the
654 MAF representing the surface expression of a gravity-driven deformation zone related to DGSD,
655 rather than an active fault. However, in our opinion, a tectonic origin is the most convincing
656 interpretation based on the following reasons.

657 1. As previously discussed (Section 2), new high-quality earthquake data define a seismically
658 active fault geometrically and kinematically compatible with the MAF (Valoroso et al., 2009). This
659 is a primary clue to the tectonic origin of the MAF.

660 2. Although DGSD are well documented in the central and northern Apennines (Galadini,
661 2006; Moro et al., 2007; Moro et al., 2009), no large-scale deep-seated gravitational deformation is
662 reported for the investigated area in literature. A possible gravitational origin of the MAF was
663 already discussed by Maschio et al. (2005), who discarded this interpretation based on geomorphic
664 analyses.

665 3. In the Central Apennines, where DGSD have been accurately investigated (see Galadini,
666 2006), they are found to develop along the slope of carbonate ridge characterized by a significant
667 relief energy, which creates the condition for increased slope instability. The increase of relief
668 energy can be a direct response to the incision of the hydrographic network caused by the regional
669 Quaternary uplift or to the long-term activity of range-bounding active normal faults. These
670 conditions do not pertain to the MAF. It does not bound a mountain front with a significant relief
671 energy, rather it is nested within the Monti della Maddalena ridge (Fig. 2). The fault, with negligible
672 cumulated vertical displacement, locally shows a tendency toward a reversal of the relief, as
673 documented by the higher elevation of the down-thrown northeastern block with respect to the
674 southwestern one (see Monte Aquila and Serra Macchitelle in Fig. 5a). Furthermore, the ~ 18 km
675 long MAF cuts across different lithologies, including limestone, shale and cherts (Fig. 2 and Fig.

676 5a; Maschio et al., 2005).

677 Relying on the above clues to a tectonic origin of the MAF, we can investigate the
678 seismological parameters of the fault. Trenching and physical logging of cores, carried out along a
679 1.2-km-long section of the MAF, allow the estimation of a minimum vertical offset for individual
680 co-seismic events. In addition, at Fornace site, a short-term cumulative vertical offset of 1.8 m can
681 be measured for the faulted bedrock (Fig. 7). If we extrapolate the displacement behavior inferred
682 by physical logging of cores (30-40 cm vertical slip per event) and assume characteristic amount of
683 displacement for event at this site (Schwartz and Coppersmith, 1984), the 1.8 short-term cumulative
684 vertical offset of the bedrock could be explained by up to 5-6 surface faulting/warping earthquakes.

685 Although we are aware of the methodological limitations, the fact that surface offsets inferred
686 from scarp profiles (Figs. 6a-c and Fig. 7) consistently indicate upper bounds between 2 and 3 m
687 suggests that multiple recent earthquakes have ruptured the whole studied section of the MAF up to
688 the surface. Following a similar reasoning and given the vertical slip per event (30-70 cm) derived
689 from paleoseismological investigations, we conjecture that 35 to 100 earthquakes occurred along
690 the MAF in order to take account for its long-term cumulative vertical displacement (25-30 m).

691 Unfortunately, paleoseismological analysis suffers from the lack of reliable age constraints for
692 all the recognized events but the more recent one, bracketed between 2.5-0.6 ka., which translates
693 into a lack of information about recurrence interval and slip rate. Our reconstruction of the past
694 history of the fault is therefore limited to a rough estimation of the age, obtained by assuming a
695 reasonable recurrence interval. If we combine the reference recurrence interval (2 ka) derived by
696 paleoseismological appraisals for large normal faults in the Apennines (Galli et al., 2008), with the
697 inferred maximum number of 100 earthquakes, we speculate that the timing of fault inception
698 should be younger than ~200 ka. Thus, under the assumption the MAF behaves as other
699 seismogenic normal faults in the Apennines (Galli et al., 2008), this fault would represent a very
700 young structure. We note that Zembo et al. (2009) recently attributed the beginning of normal
701 faulting activity along the Monti della Maddalena ridge to the latest Middle Pleistocene, specifically

702 to MIS Stage 6 (e.g. ~180 ka). A latest Middle Pleistocene age of fault inception was also proposed
703 for the Irpinia Fault by integrating geomorphic and geophysical investigations by Ascione et al.
704 (2003).

705 The clues to co-seismic surface ruptures described in this study comes from a 5-km-long
706 section of the northern fault segment (Fig. 4). The occurrence of surface faulting events along a
707 crustal fault implies large earthquakes, exceeding M6 (McCalpin, 1996; Yeats et al., 1997), which
708 involve fault segments for a minimum total length of ~10 km (Wells and Coppersmith, 1994).
709 Consistency with globally acknowledged scaling laws for active faulting parameters requires that
710 also the remaining section of the northern segment and/or the two smaller segments located
711 southeastward (Fig. 2), should have ruptured during the events singled out in this study.

712 The new earthquake data (Valoroso et al., 2008; Valoroso et al., 2009) provide valuable
713 information on the fault dimension, and back the contention that other segments of the MAF are
714 seismically active. The length of the active structure inferred from 3D earthquake locations ranges
715 from 6 km, if we only consider the intense seismicity spatially associated with the two southern
716 segments, to 12 km when we consider the remaining 15 events associated to the northern segment
717 (shown in red in Fig. 3a). Assuming a fault length between 6 and 12 km, regression relationships
718 between fault dimensions and magnitude (M_w from surface rupture length, SRL; Wells and
719 Coppersmith, 1994) provide a moment magnitude $M_w=5.8-6.3$. Similarly, if we use the regression
720 relations between fault length and moment magnitude determined for normal-faulting earthquakes
721 in the Apennines ($M_w= 4.7248L^{0.1046}$; see Galli et al., 2008), we obtain $M_w=5.7-6.2$, in good
722 agreement with the first M_w estimation. We stress that a $M_w=6.3$ event resulting from the
723 activation of a 12-km-long segment is consistent with the magnitude threshold set for surface-
724 rupturing normal events in the Apennines in the Italian Catalogue of Paleoeearthquakes (Galli et al.,
725 2008).

726 Clearly, these magnitudes could be underestimated since we limited our calculation to fault
727 dimensions inferred by microseismicity, whereas the MAF was traced by Maschio et al. (2005) for

728 a total length of ~18 km (Fig. 2). This length translates into a moment magnitude $M_w=6.5$, which is
729 more compatible with the 50-70 cm of maximum displacement per event estimated by
730 paleoseismological analyses (Wells and Coppersmith, 1994).

731 According to Maschio et al. (2005), the MAF might rupture during a larger earthquake also
732 involving the northern fault branch of the ~30-km-long MMFS (Fig. 2). However, our
733 paleoseismological data are insufficient to propose such a multiple-rupture scenario for the 1857
734 destructive earthquake ($M \sim 7$). Radiometric dating constrains a single deformation event between
735 2.5-0.6 ka, more probably closer to the older bound. As a working hypothesis, we speculate that
736 event 1 recognized in the Trincea site might correspond to the 1857 earthquake, considering the
737 southernmost active splays and the related younger colluvial wedge (Unit B, post-event 1 deposit)
738 are covered by the active soil (~20 cm thin; Fig. 13). Hence, our paleoseismological data cannot
739 definitively solve the debate on the source of the 1857 earthquake.

740

741 7. Conclusions

742

743 The integration of geologic field surveys with geophysical imaging gave compelling constraints
744 to trace the MAF with a high level of confidence, to image the shallow architecture of the fault, to
745 assess the cumulative vertical slip.

746 By a methodological point of view, this study emphasizes the benefits of using
747 multidisciplinary and multiscale approaches for shallow fault imaging. Surveys carried out in the
748 Trincea and Fornace sites represent two illuminating examples because performance of each
749 geophysical technique was markedly different in the two sites and very dependent on the local
750 geological conditions (Figs. 8 and 10). These results have wide potential implications since our
751 integration of ERT with seismic tomography is innovative, while the combination of ERT and
752 seismic reflection imaging is very rare in the existing literature (Wise et al., 2003; Ahmad et al.,
753 2009). Of particular relevance, VHR seismic and electrical resistivity tomography defined buried

754 colluvial packages, which are considered diagnostic of repeated episodes of co-seismic surface
755 faulting, a trait documented so far in a very few instances in the Basin and Range Province (Morey
756 and Schuster, 1999; Mattson, 2004, Mercur Fault; Sheley et al., 2003, Oquirrh Fault).

757 We illustrated that laboratory physical logging of cored sediments, commonly applied to
758 marine and lacustrine deposits, can be effective to investigate recent faulting in unconsolidated
759 continental sediments. In this perspective, physical logging of cored sediments might provide a
760 viable alternative when sediment characteristics prevent reliable stratigraphical correlations and/or
761 trenching is impractical.

762 Paleoseismological data indicate at least three events of displacement during the latest
763 Pleistocene (< 20 ka) and Holocene. Relying on geological (Maschio et al., 2005) and seismological
764 (Valoroso et al., 2009) clues to the tectonic origin of the MAF, we related these events of
765 displacement to co-seismic surface-faulting episodes. The occurrence of surface faulting
766 earthquakes, together with the fault dimension estimated by geological mapping and accurate
767 earthquake locations, suggest a seismogenic potential of M6.3. We stress that in Italy, the
768 occurrence of a M6.3 earthquake can produce destructive effects, as proved by the 2009 Mw 6.3
769 L'Aquila earthquake with 307 casualties.

770 Our results document that an active fault characterized by a small (25-30 m) cumulative
771 vertical displacement and subtle morphological expression, is nested within the Monti della
772 Maddalena range, to the west of the Val d'Agri large intermontane basin. These attributes make the
773 MAF similar to the Irpinia Fault (Pantosti and Valensise, 1990). By showing that the Irpinia Fault is
774 not an isolated occurrence, we claim that multidisciplinary approaches combining geologic,
775 paleoseismological and geophysical investigations are required to define a reliable framework of
776 active faults in the Southern Apennines.

777 In a wider context, the multidisciplinary and scale-based investigation strategy used in this
778 study can be effective to detect properly young and/or slow-slipping active normal faults, in regions
779 where geological and environmental conditions are unfavorable to the preservation of short-term

780 tectonic indicators (Rhine Graben, Megharoui et al., 2000; Andean Precordillera of Western
781 Argentina, Fazzito et al., 2009; Central Andes, Cabrera and Sebrier, 1998; Schoenbohm and
782 Strecker, 2009; Thessaly in Greece, Caputo, 1995), as well as in urbanized areas (Dolan and Pratt,
783 1997; Liberty et al., 2003).

784

785

786 APPENDIX A

787 Physical properties measurements: automated non-destructive HR multi-sensor core
788 logging for volume magnetic susceptibility, GRAPE density, reflectance % and P-wave
789 velocity.

790

791 Physical properties of rocks and deposits are considered as good indicators of sediment's
792 composition, formation and environmental conditions (among many others see Kim et al, 2001;
793 Casas et al., 2006). Our laboratory physical logging of cored sediments started collecting magnetic
794 susceptibility data for the FC-06 and FC-08 cores (Fig. 7) by using a Bartington MS2C loop sensor,
795 which enables to measure magnetic susceptibility on whole cores. The two magnetic susceptibility
796 logs showed comparable trends (Figure S5). Thus, we tried to correlate prominent and highly
797 informative peaks, troughs and characteristic patterns.

798 Then, in the way to refine our observations, we used a Multi-Sensor Core Logger (MSCL),
799 commonly used with deep oceanic cores, which enables physical properties measurements to be
800 made on both whole cores and split cores. Most stratigraphic applications of MSCL logs rely on the
801 relative values of logged parameters measured on marine sediments for detecting geologic events
802 (among many others see Iorio et al., 2004, Iorio et al., 2009).

803 The standard configuration of the used GEOTEK Multi-Sensor Core Logger (MSCL-S)
804 includes: (1) a Bartington MS2E Point sensor, to measure the low field magnetic susceptibility, (2)

805 a Gamma Ray Attenuation Porosity Evaluator (GRAPE) sensor to determine the bulk density, (3) a
806 Minolta Spectrophotometer CM 2002 to measure the reflectance parameter, L% (the percentage of
807 reflected energy in 10 nm wavelength steps), and (4) two Acoustic Rolling Contact (ARC)
808 transducers to evaluate the P-wave velocity.

809 The MSCL-S configuration used in this work is floor mounted on legs. A rail and pusher system
810 automatically measures the length of each core section and pushes it through the stationary sensor
811 array with sensor measurements taken at spatial increments defined by the user. Sequential core
812 sections can be loaded onto the rails. In this way, a complete core can be logged in a continuous
813 process while both the raw and processed data are graphically displayed in real time on a computer
814 display. Generally, individual core sections between 50 and 150 mm in diameter and up to 1.55 m
815 long can be logged at spatial intervals as small as a few millimeters. Fully automated core logging
816 procedures are easily controlled using standard and adapted software packages.

817 Comparison between Bartington MS2C (loop sensor) and MS2E (point sensor) allowed us
818 highlighting both differences and similarities in magnetic susceptibility signals (Fig. S5). We noted
819 that loop sensor logs are generally smoothed with respect to point sensor logs, but macroscopic
820 variations are recognizable indifferently in both signals. We found that point sensor is more
821 effective because of the highest resolution (1 cm) of the measurement. On the other hand, the
822 highest frequency characteristic of this signal complicates the visualization of the logs and
823 consequently the data analysis and the correlation.

824 In the following, we describe Gamma Density, P-wave velocity and Reflectance % logs for the
825 FC-06 log (Fig. S6). The Gamma Density log ranges between 1.9 and 2.5 g/cm³ (column A) and
826 displays a general trend dominated by evident peaks and troughs. We identify the following main
827 features: at ~0.3 m depth a rapid increase from 2.1 to 2.4 g/cm³; from 0.4 to 1.0 m three positive
828 bumps with values ~2.4 g/cm³, from 1.0 to 2.1 m a general decreasing trend; from 2.1 to 2.2 m an
829 abrupt increase from 1.9 to 2.3 g/cm³; from 2.2 to 3.8 m a plateau (a.v. ~2.3 g/cm³) with overlapped
830 a single prominent peak at 2.9 m.

831 The P-wave velocity log (column B) shows relatively high values confined in a narrow interval
832 (1400-1800 m/s), and a high-frequency content with small peaks and trough. We identify the
833 following trend: from 0 to 1.9 m a general upward trend (from 1500 to 1800 m/s), with overlapped a
834 weak peak at ~0.6 m and a bump at 1.0-1.2 m ($V_p \sim 1800$ m/s); from 1.9 to 2.8 m a decreasing trend
835 followed by a plateau (a.v. ~ 1700 m/s); from 2.8 to 3.0 m a rapid decrease down to 1400 m/s; from
836 3.0 m to final depth values in the 1500-1600 m/s range.

837 Column C shows Reflectance % data, ranging between 8% and 22%, for a wavelength of 550
838 nm. We note that peaks are relatively small and recognize the following trend: from 0 to 1.3 m a
839 general upward trend, with values increasing from 10% to 22%; from 1.3 to 2.0 m a downward
840 trend followed by trough at 2.1 m with a value $\sim 9\%$; from 2.2 to 3.3 m a plateau with a.v. of $\sim 12\%$;
841 from 3.3 to 3.9 m a bump (14% a.v.).

842 The carefully inspection and comparison of the Gamma Density, P-wave velocity and
843 Reflectance % logs allows to better constrain the homologous points (22) previously recognized on
844 the highly informative magnetic susceptibility logs (Fig. 15). We found 10 correlated piercing
845 points in the density log, whereas the correlations for P-wave velocity and total reflectance
846 furnished only 5 and 8 homologous points, respectively (Fig. S6). This latter result is probably due
847 to: a) the significant influence of the water content on P-wave velocity and reflectance %; b) the
848 high-frequency content of the P-wave velocity log.

849

850 Acknowledgments

851 We thank the Editor Robert Nowack, Hanafy Sherif and three anonymous reviewers for the
852 constructive revisions. We gratefully acknowledge Daniela Pantosti for her constructive comments
853 that have substantially improved the manuscript, and Luisa Valoroso for providing us 3D
854 hypocentral locations. Finally, we thank Antonio Rovelli and Enzo Boschi for their continuous
855 encouragements.

856

857 REFERENCES

858

859 Ahmad, J., D.R. Schmitt, C.D. Rokosh, and J.G. Pawlowicz (2009), High-resolution seismic and
860 resistivity profiling of a buried Quaternary subglacial valley: Northern Alberta, Canada, *Geological*
861 *Society of America Bulletin*, November 2009, 121, 11-12, 1570-1583.

862

863 Ascione, A., A. Cinque, L. Improta, and F. Villani (2003), Late Quaternary faulting within the
864 Southern Apennines seismic belt: new data from Mt. Marzano area (Southern Italy), *Quaternary*
865 *International*, 101-102, 27-41.

866

867 Bagnaia, R., A. D'Epifanio, and S. Sylos Labini (1992), Aquila and Subequan basins: An example
868 of Quaternary evolution in central Apennines, Italy, *Quat. Nova*, 2, 187– 209.

869

870 Barchi, M., A. Amato, G. Cippitelli, S. Merlini, and P. Montone (2007), Extensional tectonics and
871 seismicity in the axial zone of the Southern Apennines, *Boll. Soc. Geol. It. (Ital. J. Geosci.)*, Spec.
872 Issue 7, 47-56.

873

874 Benedetti, L., P. Tapponier, G. C. P. King, and L. Piccardi, (1998), Surface rupture of the 1857
875 southern Italian earthquake, *TerraNova*, 10(4), 206–210.

876

877 Boenzi F., D. Capolongo, G. Cecaro, E. D'Andrea, S. I. Giano, M. Lazzari, and M. Schiattarella
878 (2004), Evoluzione geomorfologica polifasica e tassi di sollevamento del bordo sud-occidentale
879 dell'alta Val d'Agri (Appennino meridionale), *Boll. Soc. Geol. It.*, 123, 357-372.

880

881 Boncio, P., G. Lavecchia, and B. Pace (2004), Defining a model of 3D seismogenic sources for

882 Seismic Hazard Assessment applications: The case of central Apennines (Italy), *J. Seismol.*, 8, 407–
883 425, doi:10.1023/B:JOSE.0000038449.78801.05.

884

885 Bucci, F., D. D’Onofrio, E. Tavernelli, and G. Prosser (2007), Triangula Facets or Flatirons? A note
886 of caution from the Lucanina Apennines, Italy, *Rend. Soc. Geol. It.*, 5, Nuova Serie, 91.

887

888 Bucci, F. (2009), Growth and Dissection of a Collisional Chain: Tectonic Evolution of the Southern
889 Apennines within the High Agri valley (Basilicata, Italy) Deformative Record, *Phd Thesis*, 21st
890 Course at Dept. of Earth Sciences, University of Siena, Italy.

891

892 Burrato, P., and G. Valensise (2008), Rise and fall of a hypothesized seismic gap: source
893 complexity in the 16 December 1857, Southern Italy earthquake (Mw 7.0), *Bull. Seism. Soc. Am.*,
894 98, 1, 139–148, doi: 10.1785/0120070094.

895

896 Cabrera, J., and M. Sbrrier (1998), Surface Rupture Associated with a 5.3-*mb* Earthquake: The 5
897 April 1986 Cuzco Earthquake and Kinematics of the Chincheros-Qoricocha Faults of the High
898 Andes, Peru, *Bulletin of the Seismological Society of America*, 88, 1, 242-255.

899

900 Caputo, R. (1995), Inference of a seismic gap from geological data: Thessaly (Central Greece) as a
901 case study, *Annali di Geofisica*, 38, 1, 1-19.

902

903 Caputo, R., S. Piscitelli, A. Oliveto, E. Rizzo, and V. Lapenna (2003), The use of electrical
904 resistivity tomographies in active tectonics: examples from the Tyrrhenian Basin, Greece, *J. Geodyn.*,
905 36, 1-2, 19–35.

906

907 Casas, D., G. Ercilla, V. Lykousis, I. Chryssanthi, and C. Perissoratis (2006), Physical properties

908 and their relationship to sedimentary processes and texture in sediments from mud volcanoes in the
 909 Anaximander Mountains (Eastern Mediterranean), *Scientia Marina*, 70(4), 643-659.

910

911 Castello, B., G. Selvaggi, C. Chiarabba, and A. Amato (2006), CSI Catalogo della sismicità italiana
 912 1981-2002, versione 1.1. INGV-CNT, Roma, available at <http://csi.rm.ingv.it/>.

913

914 Cello, G., R. Gambini, S. Mazzoli, A. Read, E. Tondi, and V. Zucconi (2000), The Val d'Agri fault
 915 system. In: Cello, G., Tondi, E. (Eds.), The resolution of geological analysis and models for
 916 earthquake faulting studies, *Journal of Geodynamics*, 29 (3-5), 293-308.

917

918 Cello, G., Tondi E., Micarelli L., and Mattioni L. (2003), Active tectonics and earthquake sources in
 919 the epicentral area of the 1857 Basilicata earthquake (southern Italy), *J. Geodyn.*, 36, 37-50, doi:
 920 10.1016/S0264-3707(03)00037-1.

921

922 Chiarabba C., A. Amato, M. Anselmi, et al. (2009), The 2009 L'Aquila (central Italy) Mw 6.3
 923 earthquake: Main shock and aftershocks, *Geophys. Res. Lett.*, 36, No. 18, L18308.

924

925 Cinque, A., E. Patacca, P. Scandone, and M. Tozzi (1993), Quaternary kinematic evolution of the
 926 Southern Apennines: Relationships between surface geological features and deep lithospheric
 927 structures, *Ann. Geofis.*, 36, 249-259.

928

929 Colella, A., V. Lapenna, and E. Rizzo (2004), High-resolution imaging of the High Agri Valley
 930 Basin (Southern Italy) with electrical resistivity tomography, *Tectonophysics*, 386, 29-40.

931

932 CPTI Working Group (2004), Catalogo Parametrico dei Terremoti Italiani, v. 2004 (CPTI04),
 933 INGV, Bologna, available on-line at <http://emidius.mi.ingv.it/CPTI04/>.

934

935 Cucci, L., S. Pondrelli, A. Frepoli, M. T. Mariucci, and M. Moro (2004), Local pattern of stress
936 field and seismogenic sources in the Pergola-Melandro basin and the Agri valley (Southern Italy),
937 *Geophys. J. Int.* **156**, 575–583.

938

939 D’Addezio, G., D. B. Karner, P. Burrato, D. Insinga, L. Maschio, L. Ferranti, and P. R. Renne
940 (2006), Tephrochronology in faulted Middle Pleistocene tephra layer in the Val d’Agri area
941 (Southern Italy), *Annals of Geophysics*, **49**, 4-5, 1029-1039.

942

943 DISS Working Group (2007), Database of Individual Seismogenic Sources (DISS), Version 3.0.4:
944 A compilation of potential sources for earthquakes larger than M 5.5 in Italy and surrounding areas,
945 available on-line at www.ingv.it/DISS/.

946

947 Doglioni, C., F. Mongelli, and P. Pieri (1994), The Puglia uplift (SE Italy). An anomaly in the
948 foreland of the Apenninic subduction due to buckling of a thick continental lithosphere, *Tectonics*,
949 **13**(5), 1309-1321.

950

951 Dolan, J.F., and T.L. Pratt, T.L. (1997), High resolution seismic reflection profiling of the Santa
952 Monica fault zone, West Los Angeles, California, *Geophys. Res. Lett.*, **24**, 16, 2051-2054.

953

954 Fazzito, S. Y., A.E. Papalini, J.M. Cortés, and C.M. Terrizzano (2009), Characterization of
955 Quaternary faults by electric resistivity tomography in the Andean Precordillera of Western
956 Argentina, *Journal of South American Earth Sciences*, **28**, 3, 217-228.

957

958 Ferranti L., P.R. Gialanella, F. Heller, and A. Incoronato (2005), Structural and magnetic record of
959 superposed non-coaxial deformation in the Lagonegro thrust nappe, Southern Apennines of Italy,

960 *Boll. Soc. Geol. It., (Ital. J. Geosci.), 124, 345-365.*

961

962 Galadini, F. (2006), Quaternary tectonics and large-scale gravitational deformations with evidence
 963 of rock-slide displacements in the Central Apennines (central Italy), *Geomorphology*, 82, 3-4, 201-
 964 228.

965

966 Galli, P., F. Galadini, and D. Pantosti (2008), Twenty years of paleoseismology in Italy, *Earth-*
 967 *Science Reviews*, 88, 89-117, doi:10.1016/j.earscirev.2008.01.001.

968

969 Hippolyte, J.C., J. Angelier, and F. Roure (1994), A major geodynamic change revealed by
 970 Quaternary stress patterns in Southern Apennines (Italy), *Tectonophysics*, 230, 199-210.

971

972 Improta, L., A. Zollo, A. Herrero, R. Frattini, J. Virieux, and P. Dell'Aversana, (2002), Seismic
 973 imaging of complex structures by non-linear traveltimes inversion of dense wide-angle data:
 974 application to a thrust belt, *Geophys. J. Int.*, 151, 264-278.

975

976 Improta, L., A. Zollo, P.P. Bruno, A. Herrero, and F. Villani (2003), High resolution seismic
 977 tomography across the 1980 (Ms 6.9) Southern Italy earthquake fault scarp, *Geophys. Res. Lett.*, 30-
 978 10.

979

980 Improta, L., and M. Corciulo (2006), Controlled source non-linear tomography: a powerful tool to
 981 constrain tectonic models of the Southern Apennines orogenic wedge, Italy. *Geology*, 34, n°11,
 982 941-944.

983

984 Iorio, M., L. Sagnotti, A. Angelino, F. Budillon, B. D'Argenio, J. Dinares-Turell, P. Macrì, and E.
 985 Marsella (2004), High resolution petrophysical and palaeomagnetic study of late-Holocene shelf

986 sediments, Salerno Gulf, Tyrrhenian sea, *The Holocene* 14, 3, 426-435.

987

988 Iorio, M., Liddicoat, J., Budillon, F., Tiano, P., Incoronato, A., Coe, R. and E. Marsella (2009),

989 Palaeomagnetic Secular Variation Time Costrain on Late Neogene Geological Events in slope

990 sediment from the Eastern Tyrrhenian Sea, *SEPM (Society for Sedimentary Geology) Spec. Pub.*,

991 92, 233-243.

992

993 Kim, D.C., J.Y. Sung, S.C. Park, G.H. Lee, J.H. Choi, G.Y. Kim, Y.K. Seo, and J.C. Kim (2001),

994 Physical and acoustic properties of shelf sediments, the South Sea of Korea, *Marine Geology*, 179,

995 39-50.

996

997 Liberty, L.M., M.A. Hemphill-Halley, and I.P. Madin (2003), The Portland Hill Fault: uncovering a

998 hidden fault in Portland, Oregon using high-resolution geophysical methods, *Tectonophysics*, 368,

999 89-103

1000

1001 Loke, M.H. (2001), Tutorial: 2-D and 3-D electrical imaging surveys, in *Course Notes for USGS*

1002 *Workshop "2-D and 3-D inversion and modeling of surface and borehole resistivity data"*, Storrs,

1003 CT, 13–16 March 2001.

1004

1005 Malinverno, A., and W.B.F. Ryan (1986), Extension in the Tyrrhenian Sea and shortening in the

1006 Apennines as a result of arc migration driven by sinking of the lithosphere, *Tectonics*, 5, 227-245.

1007

1008 Maschio, L., L. Ferranti, and P. Burrato (2005), Active extension in Val d'Agri area, Southern

1009 Apennines, Italy: implications for the geometry of the seismogenic belt, *Geophys. J. Int.*, 162 (2),

1010 591–609, doi:10.1111/j.1365-246X.2005.02597.x.

1011

1012 Mattson, A. (2004), Tomographic imaging of late Quaternary faulting, Oquirrh Mountains, Utah, *J.*
1013 *Geophys. Res.*, *109*, B11310, doi:10.1029/2004JB003159.

1014

1015 Mazzoli, S., S. Barkham, G. Cello, R. Gambini, L. Mattioni, P. Shiner, and E. Tondi (2001),
1016 Reconstruction of continental margin architecture deformed by the contraction of the Lagonegro
1017 Basin, Southern Apennines, Italy, *J. Geol. Soc. London*, *158*, 309-319.

1018

1019 Mc Calpin, J.P. (Ed.) (1996), Paleoseismology, Academic Press, San Diego, 588 pp.

1020

1021 Mc Calpin, J.P. (Ed.) (2009), Paleoseismology, Academic Press, Second Edition, 629 pp. ISBN:
1022 0123735769.

1023

1024 Meghraoui, M., T., K. Camelbeeck, K. Vanneste, M. Brondeel, and D. Jongmans (2000), Active
1025 faulting and paleoseismology along the Bree fault, lower Rhine graben, Belgium, *J. Geophys. Res.*,
1026 *105(B6)*, 13809-13841.

1027

1028 Michetti, A.M., L. Ferrelli, E. Esposito, S. Porfido, A. M. Blumetti, E. Vittori, L. Serva, and G. P.
1029 Roberts (2000), Ground effects during the 9 September, 1998, Mw 4.5, L'Aquila earthquake and the
1030 seismic potential of the "Aseismic" Pollino region in Southern Italy, *Seismological Research*
1031 *Letters*, *71*, 31-46.

1032

1033 Miller, R.D., D.W. Steeples, and P.B. Myers (1990), Shallow seismic reflection survey across the
1034 Meer Fault, Oklahoma, *Geol. Soc. Am. Bull.*, *102*, 18-25.

1035

1036 Montone, P., M. T. Mariucci, S. Pondrelli, and A. Amato (2004), An improved stress map for Italy
1037 and surrounding regions (central Mediterranean), *J. Geophys. Res.*, *109*, B10410,

doi:10.1029/2003JB002703.

Morey, D., and G.T. Schuster (1999), Paleoseismicity of the Oquirrh fault, Utah, from shallow seismic tomography, *Geophys. J. Int.*, 138, 25-35.

Moro, M., M. Saroli, S. Salvi, S. Stramondo, and F. Doumaz (2007), The relationship between seismic deformation and deep-seated gravitational movements during the 1997 Umbria-Marche (Central Italy) earthquakes, *Geomorphology*, 89, 297-307.

Moro, M., M. Saroli, C. Tolomei, and S. Salvi (2009), Insights on the kinematics of deep-seated gravitational slope deformations along the 1915 Avezzano earthquake fault (Central Italy), from time-series DInSAR, *Geomorphology*, 112, 261-276.

Nguyen, F., S. Garambois, D. Jongmans, E. Pirard, and M.H. Loke (2005), Image processing of 2D resistivity data for imaging faults, *Journal of Applied Geophysics*, 57, 260-277.

Pantosti, D., and G. Valensise (1990), Faulting mechanism and complexity of the November 23, 1980, Campania-Lucania earthquake, inferred from surface observations, *J. Geophys. Res.*, 95, B10, 15,319-15,341.

Pantosti, D., D. Schwartz, G. Valensise (1993), Paleoseismology along the 1980 surface rupture of the Irpinia Fault; implications for earthquake recurrence in the Southern Apennines, Italy, *J. Geophys. Res.*, 98, B4, 6561-6577.

Pastori M., D. Piccinini, L. Margheriti, L. Improta, L. Valoroso, L. Chiaraluce, and C. Chiarabba (2009), Stress aligned cracks in the upper crust of the Val d’Agri region as revealed by Shear Wave

1064 Splitting, *Geophys. J. Internat.*, 179, Issue 1, 601-614.

1065

1066 Patacca, E., R. Sartori, and P. Scandone (1990), Tyrrhenian basin and Apenninic arcs: kinematics
1067 relations since late Tortonian times, *Mem. Soc. Geol. It.*, 45, 425-451.

1068

1069 Pondrelli, S., S. Salimbeni, G. Ekström, A. Morelli, P. Gasperini, and G. Vannucci (2006), The
1070 Italian CMT dataset from 1977 to the present, *Phys. Earth Planet. Int.*,
1071 doi:10.1016/j.pepi.2006.07.008, 159/3-4, 286-303.

1072

1073 Schoenbohm, L.M., and R. Strecker (2009), Normal faulting along the southern margin of the Puna
1074 Plateau, northwest Argentina, *Tectonics*, 28, TC5008, doi:10.1029/2008TC002341.

1075

1076 Schwartz, P.D., K. J. Coppersmith (1984), Fault behavior and characteristic earthquakes: examples
1077 from the Wasatch and San Andreas Fault, *J. Geophys. Res.*, 89, 5681–5698.

1078

1079 Serpelloni, E., M. Anzidei, P. Baldi, G. Casula, and A. Galvani (2005), Crustal velocity and strain
1080 rate fields in Italy and surrounding regions: new results from the analysis of permanent and
1081 nonpermanent GPS networks, *Geophys. J. Int.*, 161, 861–880.

1082

1083 Sheley, D., T. Crosby, M. Zhou, J. Giacomini, J. Yu, R. He, and G.T. Schuster (2003), 2-D seismic
1084 trenching of colluvial wedges and faults, *Tectonophysics*, 368, 51-69.

1085

1086 Steeples, D.W., and R.D. Miller (1998), Avoiding pitfalls in shallow seismic reflection surveys.
1087 *Geophysics*, 63, 1213-1224.

1088

1089 Stuiver, M., and P.J. Reimer (2005), Radiocarbon calibration program CALIB REV5.0.2, copyright,

1090 available at <http://calib.cub.ac.uk/calib/>.
1091
1092 Suzuki, K, S. Toda, K. Kusunoki, Y. Fujimitsu, T. Mogi, A. Jomori (2000), Case studies of
1093 electrical and electromagnetic methods applied to mapping active faults beneath the thick
1094 quaternary, *Eng. Geol.*, 56, 29–45.
1095
1096 Valoroso, L., L. Improta, P. De Gori, R. Di Stefano, L. Chiaraluce, and C. Chiarabba (2008), From
1097 3D to 4D passive seismic tomography: the sub-surface structure imaging of the Val d’Agri region,
1098 southern Italy, 70th EAGE Conference and Exhibition, Suppl., Ext. Abstract, P28.
1099
1100 Valoroso, L., L. Improta, L. Chiaraluce, R. Di Stefano, L. Ferranti, A. Govoni, and C. Chiarabba
1101 (2009), Active faults and induced seismicity in the Val d’Agri area (Southern Apennines, Italy),
1102 *Geophys. J. Int.*, 178, 488-502, doi: 10.1111/j.1365-246X.2009.04166.x.
1103
1104 Wallace, R.E. (1984), Pattern and timing of late Quaternary faulting in the Great Basin province
1105 and relation to some regional tectonic features, *J. Geophys. Res.*, 89, 5763-5769.
1106
1107 Wells, D.L., and K. J. Coppersmith (1994), New empirical relationship among magnitude, rupture
1108 length, rupture width, rupture area, surface displacement, *Bull. Seism. Soc. Am.*, 84, 974-1002.
1109
1110 Westaway, R., and J.A. Jackson (1987), The earthquake of 1980 November 23 Campania-Basilicata
1111 (Southern Italy), *J. Geophy. Res.*, 90, 375-443.
1112
1113 Wise D.J., J. Cassidy, and C.A. Locke (2003), Geophysical imaging of the Quaternary Wairoa
1114 North Fault, New Zealand: a case study, *Journal of Applied Geophysics*, 53, 1-16.
1115

1116 Yeats, R.S., K. Sieh, and C. R. Allen (1997), The Geology of Earthquakes, Oxford Univ. Press, NY.
1117 568 pp.
1118
1119 Zembo, I., L. Panzeri, A. Galli, R. Berenzio, M. Martini, and E. Sibilio (2009), Quaternary
1120 evolution of the intermontane Val d'Agri Basin, Southern Apennines, *Quaternary Research*, 72, 3,
1121 431-442.

1122
1123

1124 **Figure Captions**

1125

1126 **Figure 1:** (a) Sketch map of the central Mediterranean area and location of the Apennine range. The
1127 black box outlines the area shown in panel b. (b) Map of the Southern Apennines showing historical
1128 earthquakes (squares proportional to magnitude, from CPTI Working Group, 2004) and
1129 instrumental seismicity (diamond proportional to magnitude, from Castello et al., 2006). Focal
1130 mechanisms of main events ($M > 5$) are selected from the Italian CMT dataset (Pondrelli et al.,
1131 2006; A – Irpinia 23/11/1980, M6.9; B - Irpinia, 25/11/1980, M5.3; C – Potenza, 05/05/1990, M5.7;
1132 D – Potenza, 05/05/1990, M5.0; E – San Gregorio, 03/04/1996, M5.1; F – Castelluccio, 09/09/1998,
1133 M5.6). Surface ruptures of the 1980 Irpinia earthquake are depicted by thick white lines. The white
1134 dashed circles denote the Sannio-Irpinia boundary (SIB) and the Val d’Agri (VA) region,
1135 corresponding to major seismic gaps in the instrumental catalogues (Castello et al., 2006).

1136

1137 **Figure 2:** Schematic geologic map of the Val d’Agri region showing the distribution of lithological-
1138 tectonic assemblages and Quaternary faults (modified from Maschio et al., 2005).
1139 Faults: EAFS, Eastern Agri Fault System; MMFS, Monti della Maddalena Fault System; MAF,
1140 Monte Aquila Fault shown with a thick red lines. Geology: 1, fluvio-lacustrine deposits (Holocene-
1141 upper Pleistocene); 2, fluvio-lacustrine deposits (upper-middle Pleistocene); 3, alluvial and talus

deposits (middle-lower Pleistocene); 4, marine and continental clastics (middle Pleistocene-Pliocene); 5, carbonate platform and slope rocks (Miocene-upper Triassic); 6, Lagonegro basin rocks and foredeep deposits (Miocene-middle Triassic). The dotted white line corresponds to the region of intense microseismicity identified by Valoroso et al. (2009). Macroseismic epicenter of the 1857 M7 event is outlined by a star.

Figure 3: (a) Geological map zooming on the MAF with, superimposed, accurate 3D locations of earthquakes recorded during a very dense passive seismic survey, which were related to the MAF (Valoroso et al., 2008; Valoroso et al., 2009). Earthquakes are distinguished according to hypocentral depth (blue $6.0 < Z < 9.0$ km depth; green $4.5 < Z < 6.0$ km; yellow $3.0 < Z < 4.5$ km; orange $1.5 < Z < 3.0$ km; red $Z < 1.5$ km). The three strands of the MAF are outlined with thick red lines. The trace of the cross-section shown in panel b is outlined by a blue dashed line. The black square corresponds to the extent of the map shown in Figure 4. (b) Hypocentral locations projected on a SW-NE trending profile. Focal mechanisms for four representative earthquakes are also reported. The alignment of hypocenters reveals a straight fault plane (dashed line) from 1 to 6.5 km depth. The surface projection of the plane and the kinematics (NW-trending normal faulting) are compatible with the MAF.

Figure 4: Topographic map zooming on the central part of the Monte Aquila Fault. The different morphological and structural signatures of the fault trace along strike are reported with different color code. Pseudo-focal mechanisms for the northern sector at Cava site (left), and central sector at Trincea site (right) are also reported.

Figure 5: (a) Geological and geomorphological map zooming on the Macchitelle basin showing scarps/warps associated with the MAF (red lines). Geology: 1 – recent colluvia, alluvia and carbonate debris; 2 – slope-facies limestone (Apennine platform, Mesozoic); 3 – shale (Lagonegro

basin, Cretaceous); 4 – chert and cherty-limestone (Lagonegro basin, Jurassic-Cretaceous). Thick orange lines denote overthrusting, dotted lines relics of Quaternary erosional surfaces with corresponding elevations. Location of the multidisciplinary surveys is indicated by thick black lines (S- Scarpata, T – Trincea, C - Covoni, F – Fornace), the trace of the cross-section shown in panel b by the black dashed line. (b) Schematic geologic section across the Macchitelle basin and the MAF with outlined displaced thrusts and Quaternary erosional surfaces. The location of the ERT survey in the site Trincea is also reported.

Figure 6: Topographic profiles along the MAF with cumulative displacements measured across the scarp or surface warping (a – Scarpata site, b – Trincea site, c – Covoni site). The profiles are also plotted with respect to the origin of the ERT surveys.

Figure 7: Topographic profiles along the MAF in the Fornace site, with cumulative displacement measured across the surface warping (topography is also plotted with respect to the origin of the ERT survey). Location of the boreholes, with lithological classification, is showed (A – active soil; B – coarser colluvia; C – finer colluvia; Bd – carbonate bedrock).

Figure 8: Geophysical prospecting at Trincea site

(a) ERT model: 1 – colluvia, 2 – saturated alluvia, 3 – carbonate slope debris, 4 – limestone bedrock, 5 – Lagonegro shale bedrock, Un – uncertain body with moderate resistivity. Trench position is outlined by a green thick line. A photo of the southernmost portion of the trench wall is reported. (b) Large-wavelength Vp model. The black dashed line outlines resolution depth (see Fig.S2 in auxiliary material). The extent the small-wavelength shallow model showed in panel c is traced by a yellow dotted line. The velocity nodes (model parameters) are shown by black dots. (c) Small-wavelength Vp model. The black dashed line outlines resolution depth (see Fig.S2). The position of the main fault scarp and trench (green thick line) are also reported.

1194

1195 **Figure 9:** ERT surveys at Covoni site

1196 (a) Very high-resolution shallow ERT: 1a – near-surface dry colluvial soils, 1b – saturated colluvial
1197 soils. A photo of the secondary fault recognized in trench is also reported. (b) High-resolution ERT:
1198 1 – colluvial package, 2 – saturated alluvia, 3 – limestone bedrock, 4 – Lagonegro shale bedrock.
1199 Trench position is shown by a green thick line. The extent the very high-resolution ERT model is
1200 outlined by a yellow dotted line.

1201

1202 **Figure 10:** Geophysical prospecting at Fornace site

1203 (a) Very high-resolution shallow ERT: 1a – coarser colluvia, 1b – finer colluvia, 3 – limestone
1204 bedrock. Boreholes are also reported (red - Unit A, green - Unit B, yellow - Unit C, blue - bedrock).
1205 (b) High-resolution ERT: 1 – colluvial package, 2 – saturated alluvia, 3 – limestone bedrock. The
1206 blue dashed line reports the top of the bedrock. The extent the very high-resolution shallow model
1207 showed in panel a is outlined by a black dotted line. Black triangles depict boreholes location. (c) –
1208 Large-wavelength Vp model. The black dashed line outlines resolution depth (see Fig. S4 in
1209 auxiliary material). The velocity grid is shown by black dots. The extent the small-wavelength
1210 shallow model (d) is traced by a yellow dotted line. (d) – Small-wavelength Vp model. The black
1211 dashed line outlines resolution depth (see Fig. S4).

1212

1213 **Figure 11:** Time migrated CDP stack section

1214 (a) Trincea Profile. Main reflectors: f – normal faults (blue), b – basin bedrock (dashed cyan), c –
1215 top of the limestone bedrock on the eastern side, t – old thrust, cp – colluvial package with possible
1216 top (green dashed line). The black dotted line depicts the approximate topographic surface resulting
1217 from a datum set to 22 m (the maximum relative elevation along the seismic line). The relative
1218 elevation, the trench and fault-scarp positions are showed in the upper panel. (b) Fornace Profile:
1219 Main reflectors: A – truncated events within the pre-Quaternary substratum, B and S – prominent

1220 truncated/warped shallow reflectors, D – possible disrupted zone across the fault zone. The fault
1221 trace is outlined in yellow.

1222
1223 **Figure 12:** Comparison among trench log (a), high-resolution shallow Vp model (b) and reflectivity
1224 image across the fault zone (c) in the Trincea site. “A” and “B” in panel b denote the low-Vp
1225 colluvial packages. Reflectors associated to the top of the bedrock (blue dashed lines) and of the
1226 colluvial package (yellow dashed line) are converted in depth using tomographic velocities.

1227
1228 **Figure 13:** Log of the eastern wall of Trincea site trench and related stratigraphy. **A:** fine grained
1229 light brown active soil, with bioturbation and roots; **B:** fine grained greenish silty colluvium; **C:** fine
1230 grained dark-brown silty paleosol; **D:** fine grained reddish-brown silty clay; **E:** fine grained dark
1231 brown silty-clayey paleosol; **F:** reddish-brown silty clay with light brown laminations and
1232 weathered pumices and sparse very fine calcareous-mudstone (bedrock) fragments; **G:** massive
1233 brown clay with weathered pumices and sparse fine calcareous-mudstone (bedrock) fragments. At
1234 the base chips of Unit I; **I:** massive light reddish-brown clay with fine weathered pumices and
1235 sparse minerals; **L:** dark reddish-brown vacuolar clay with conchoidal fracture and with diffused
1236 manganese concretions mainly at the top of the unit, sparse minerals and very fine sub-angular
1237 calcareous-mudstone (bedrock) fragments; **M:** massive yellowish-green clay grading to silty clay in
1238 the upper part, with fine to medium sub-angular calcareous-mudstone (bedrock) fragments; **N:**
1239 massive pinkish clay with rare rounded manganese concretions and weathered pumices, grading
1240 upward to silty clay with very fine sub-angular calcareous-mudstone (bedrock) fragments; **O:**
1241 massive reddish clay with diffused manganese concretions and very fine calcareous-mudstone
1242 (bedrock) fragments. The unit presents intercalation of pumice layers; **P:** very thin (up to 3 cm) and
1243 localized (>4m long) orange-brown ash bed composed of altered pumices; **Q:** light yellow pumice
1244 layer formed by poorly welded, medium coarse pumices, locally altered, with visible mineral
1245 grains. Maximum thickness 10 cm; **R:** massive dark brown clayey silty paleosol with sparse sub-

1246 angular calcareous-mudstone (bedrock) fragments; **S**: dark yellowish clay with sparse sub-angular
1247 calcareous-mudstone (bedrock) fragments; **T**: dark yellowish clay, reddish in the lower part, with
1248 very fine rounded manganese concretions; **U**: yellow silty clay with sub-angular calcareous-
1249 mudstone (bedrock) fragments; **V**: reddish-brown clay with diffuse manganese concretions and very
1250 fine sub-angular calcareous-mudstone (bedrock) fragments, including in the lower part a m-scale
1251 breccia block with marly-limestone, flattened clasts up to 5 cm long in silty-clay matrix; **TS**: Tephra
1252 sample dated by D'Addezio et al. (2006).

1253
1254 **Figure 14:** Log of the northwestern wall of Covoni site trench and related stratigraphy. **A1 - A2**:
1255 fine grained (silt) dark brown active soil, with roots and sparse clasts, more abundant in Unit A2; **B**:
1256 massive brown clayey silt with diffuse calcareous clasts. Next to the fault zone is visible a silty
1257 pocket with abundant clasts; **C1**: black silt with abundant charcoals and sparse clasts, possibly a
1258 paleosol; **C2**: gray-brown silt; **C3**: reddish-brown silty clay with reddish-blackish flames; **D**: yellow
1259 silty clay with few sparse clasts more abundant in the uppermost portion, with rare yellow pumices
1260 and pockets rich in darker material, probably organic; **E**: massive orange clayey silt, with yellow
1261 pumices and calcareous clasts. Diffuse manganese concretions and nodules; **F**: fine gravel and sand
1262 within reddish silty matrix; **G**: massive yellow silty clay with sparse clasts; **M**: reddish laminated
1263 clayey silt with a few sparse clasts; **N – N1**: Colluvium with heterometric clasts within silty-clayey
1264 matrix; **P**: Yellow clayey silt organized in lenses; **R**: brown clayey silt with sparse clasts and
1265 carbonate concretions at the top; **S**: light yellow clay; **T**: blocks characterized by re-precipitation of
1266 calcium.

1267
1268 **Figure 15:** Magnetic susceptibility logs for cores FC-06 and FC-08 with the 22 homologous points
1269 used for high-resolution correlation (dashed lines). Thin and thick curves represent the original (1-
1270 cm-sampling) and the smoothed log, respectively. Thick dashed lines correspond to homologous
1271 points identified in at least three of the physical logs. FC-08 log is shifted in depth since the

1272 correlation evidences that it lacks the shallower organic soils (~40 cm) because of intense
1273 ploughing. Boreholes location is reported in Figure 7.

1274
1275 **Figure 16:** Vertical offset *versus* depth in FC-08 borehole inferred from the depth difference of all
1276 the homologous piercing points identified by correlating the logs. Offset values are distinguished
1277 according to the measured physical property.

1278

1279

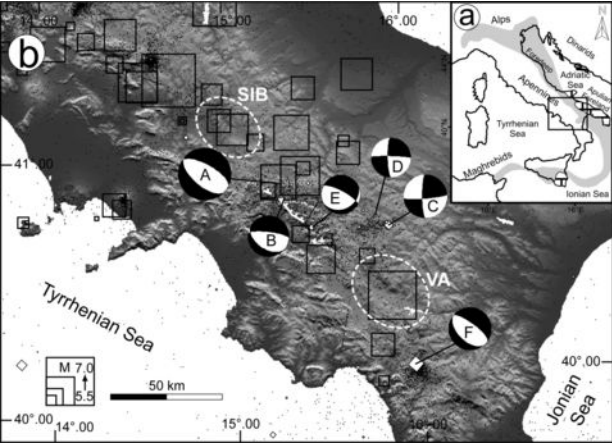
1280 **Tables**

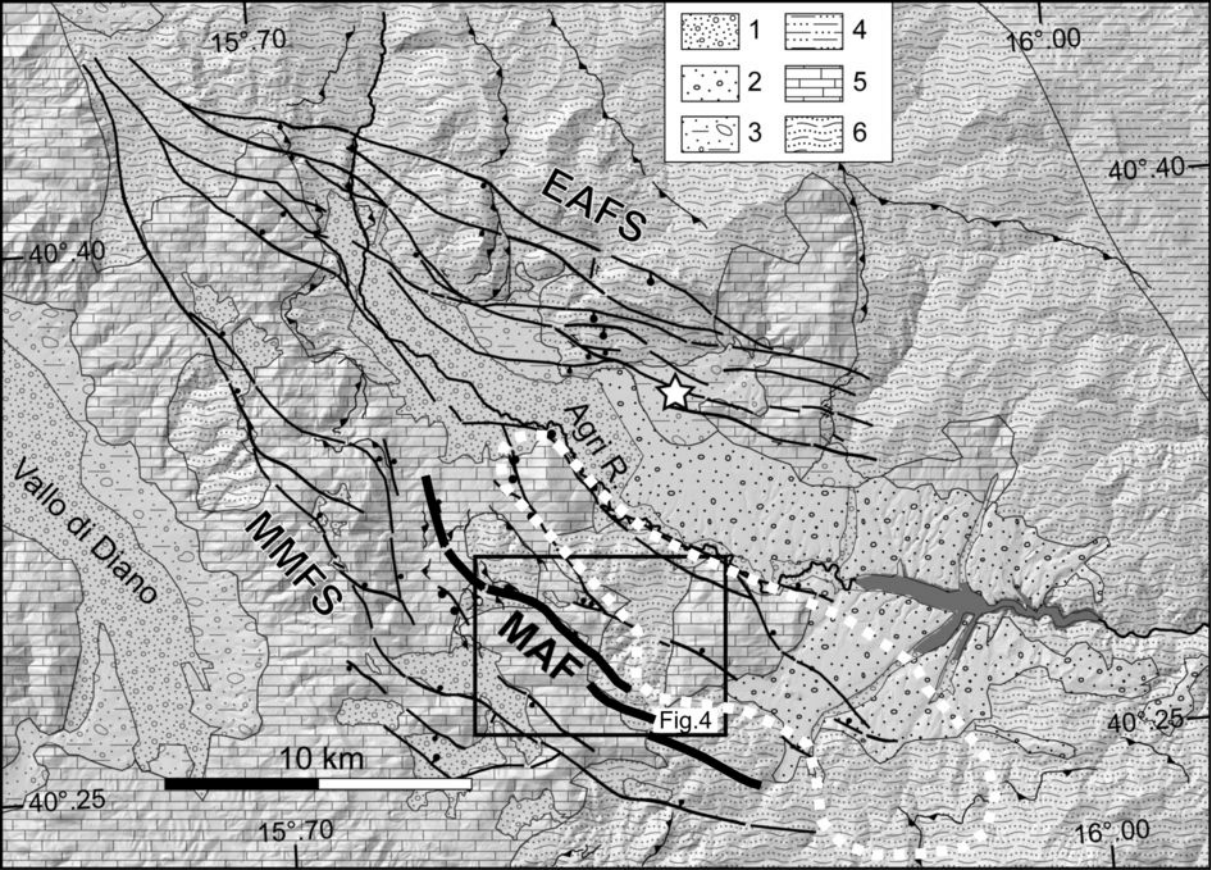
1281

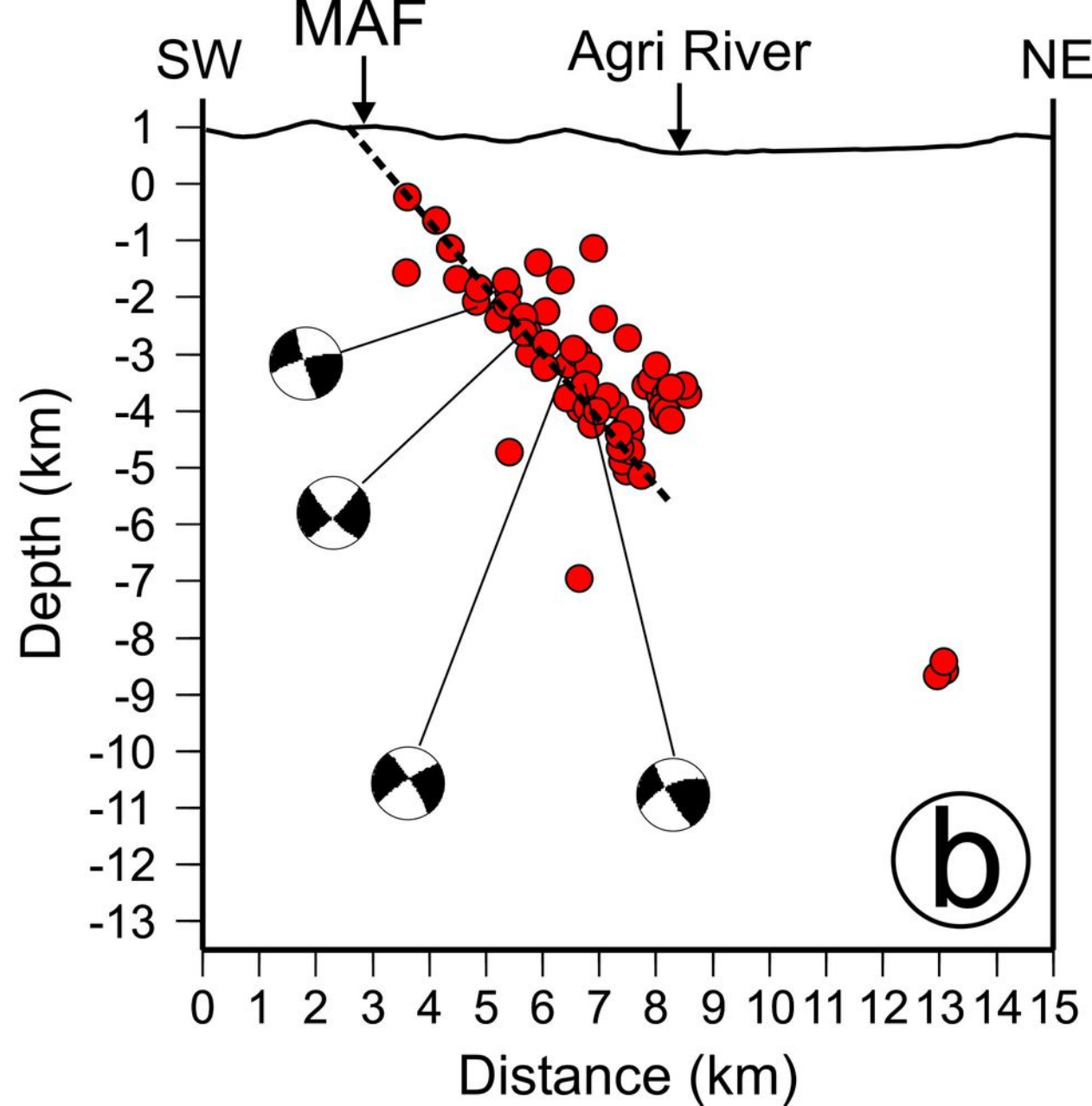
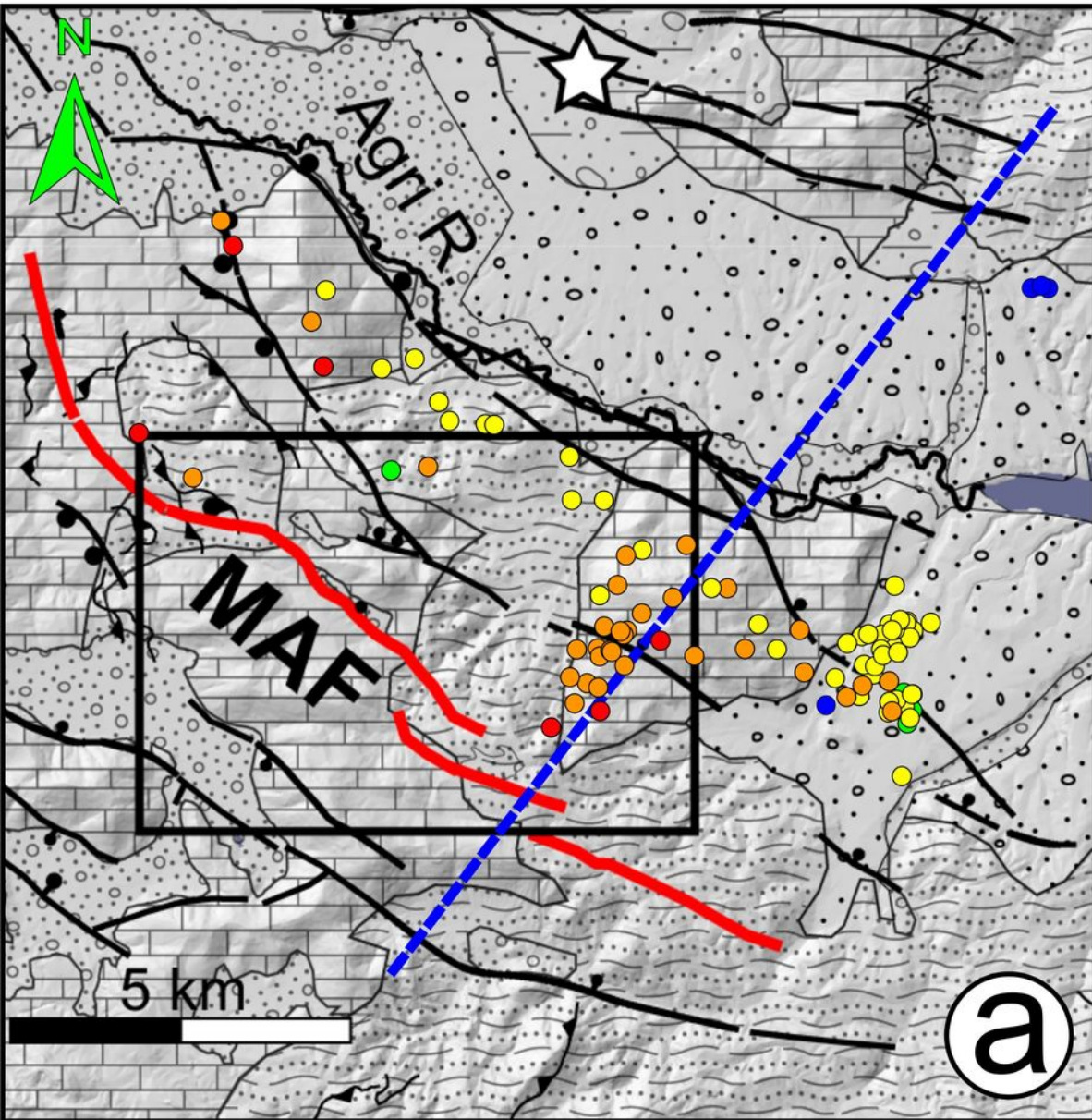
1282 **Table 1.** Field parameters used for the ERT, the seismic reflection and dense wide-aperture profiles
1283 at Trincea, Covoni and Fornace sites.

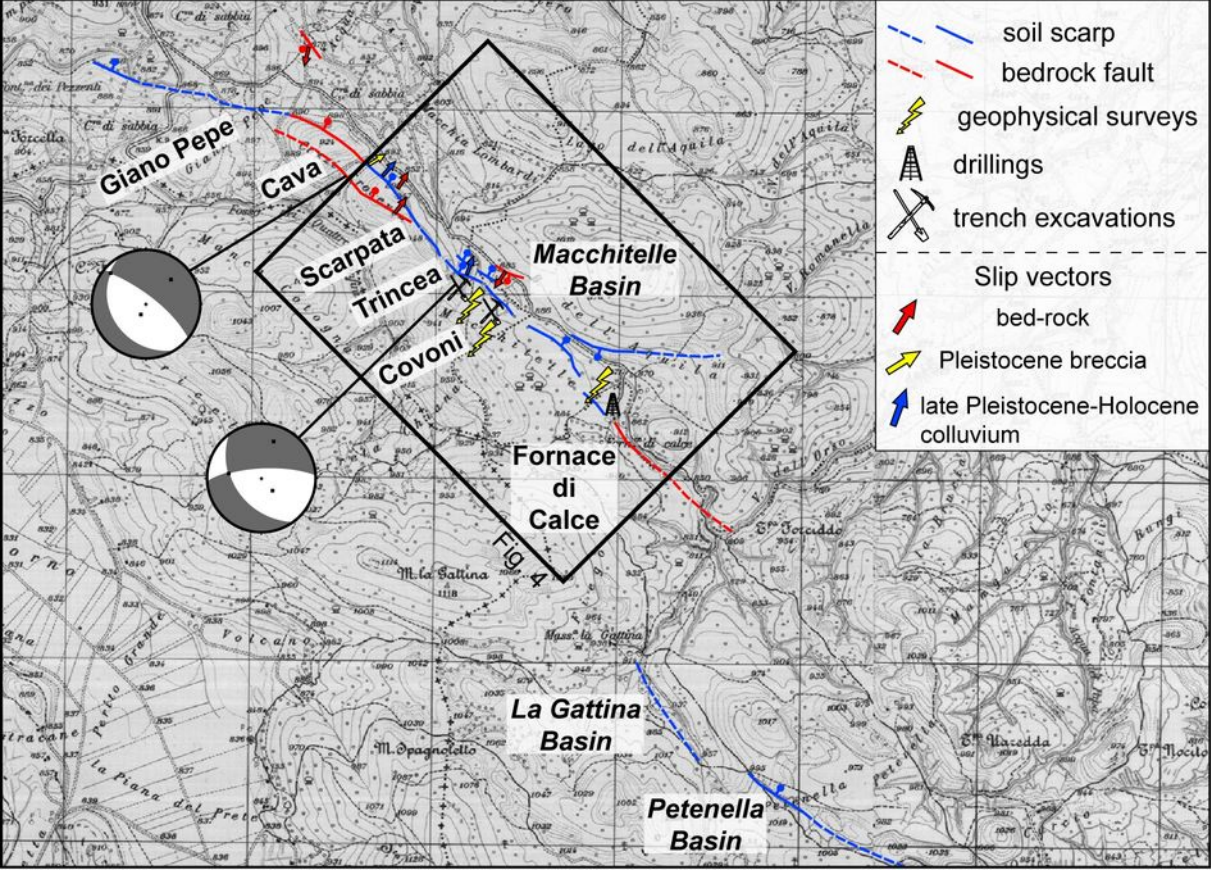
1284

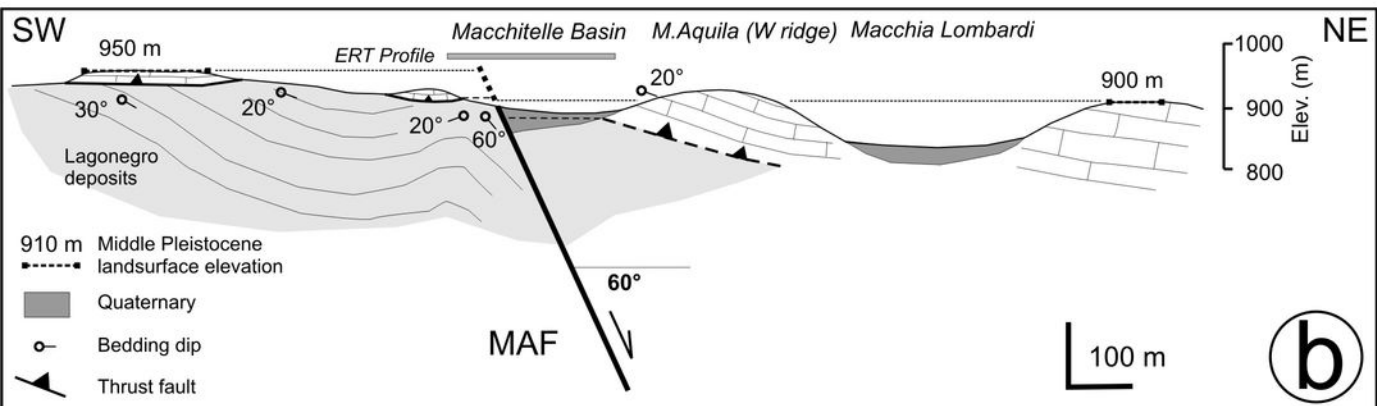
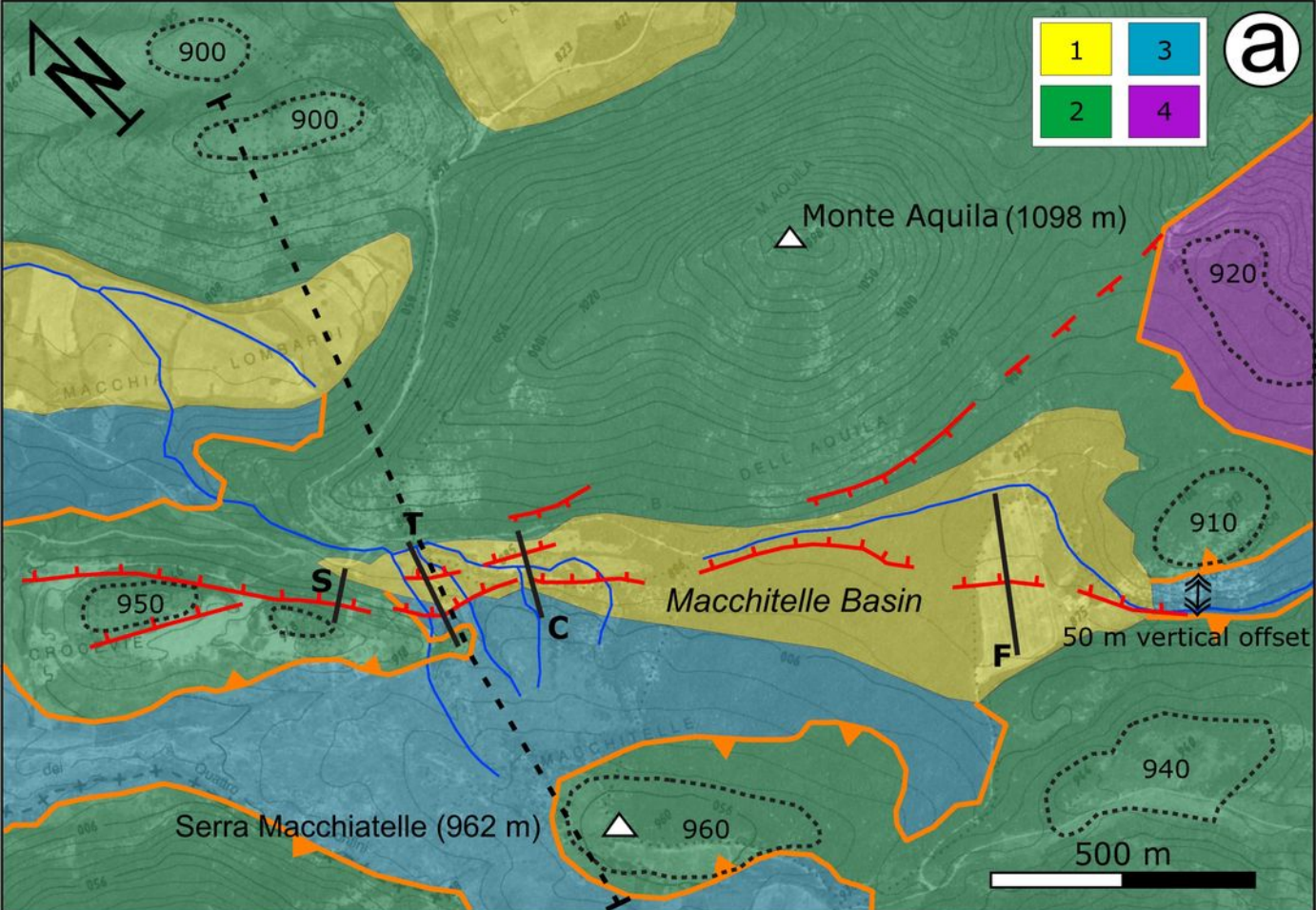
1285 **Table 2.** Measured and calibrated ages (according to Calib REV5.0.2 by Stuiver and Reimer, 2005)
1286 of samples collected in the trenches Trincea and Covoni.

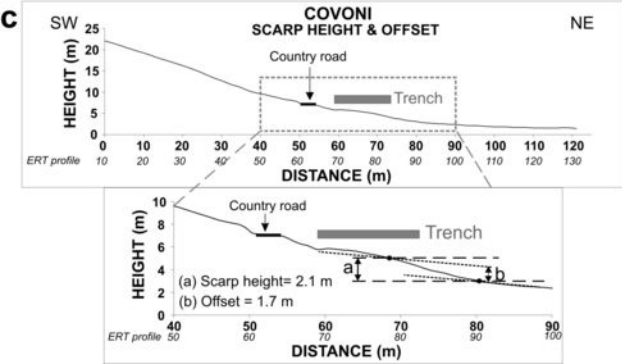
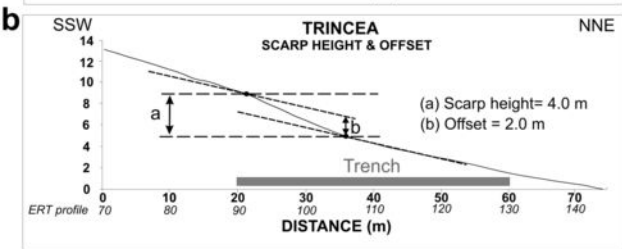
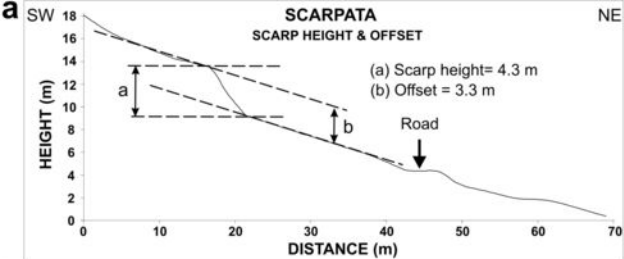


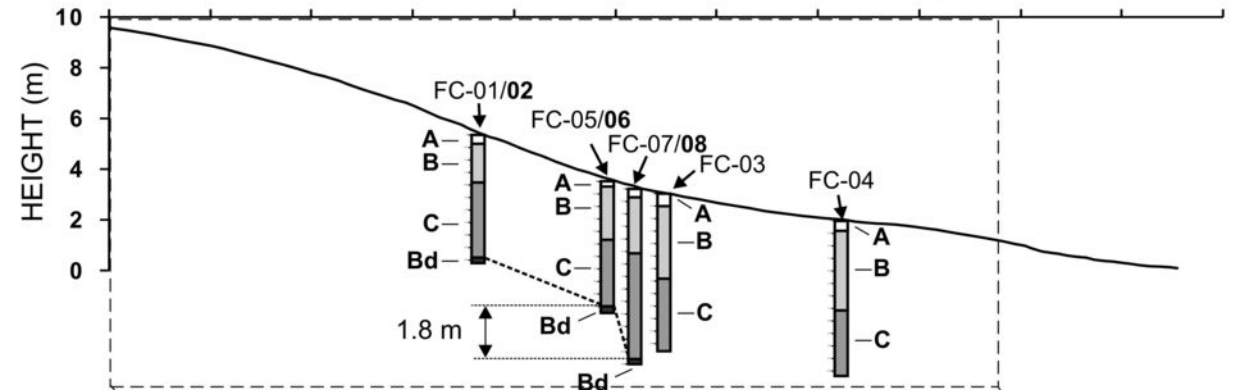
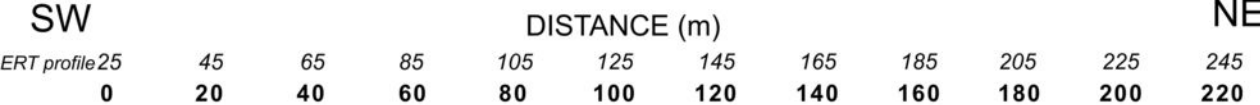




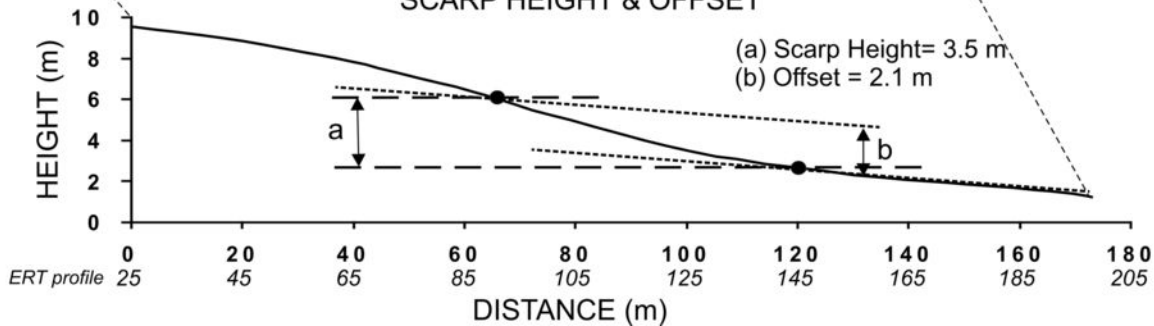


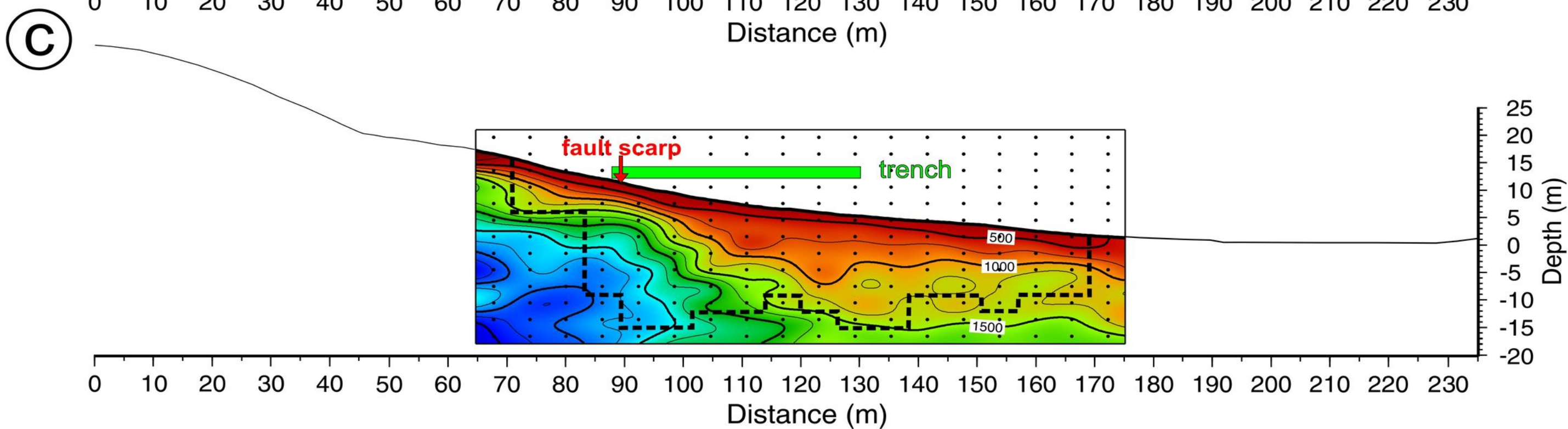
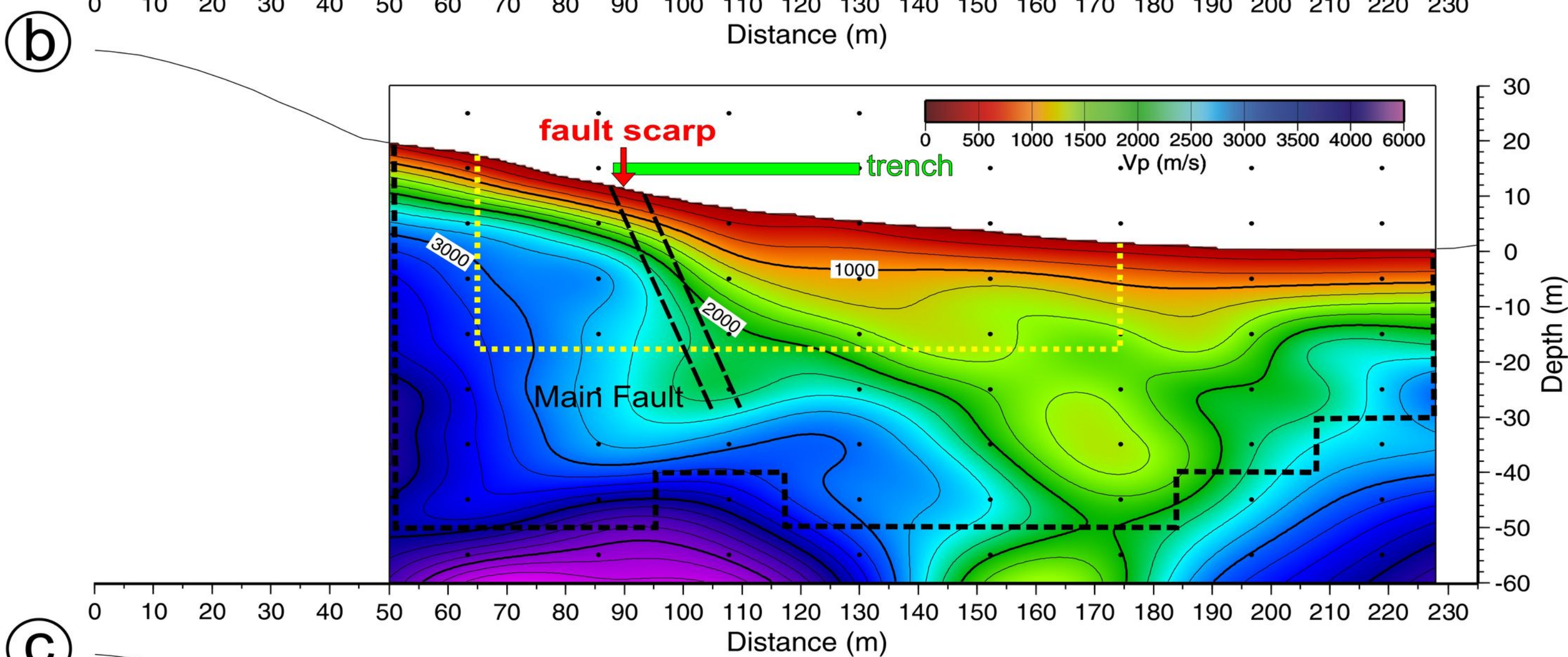
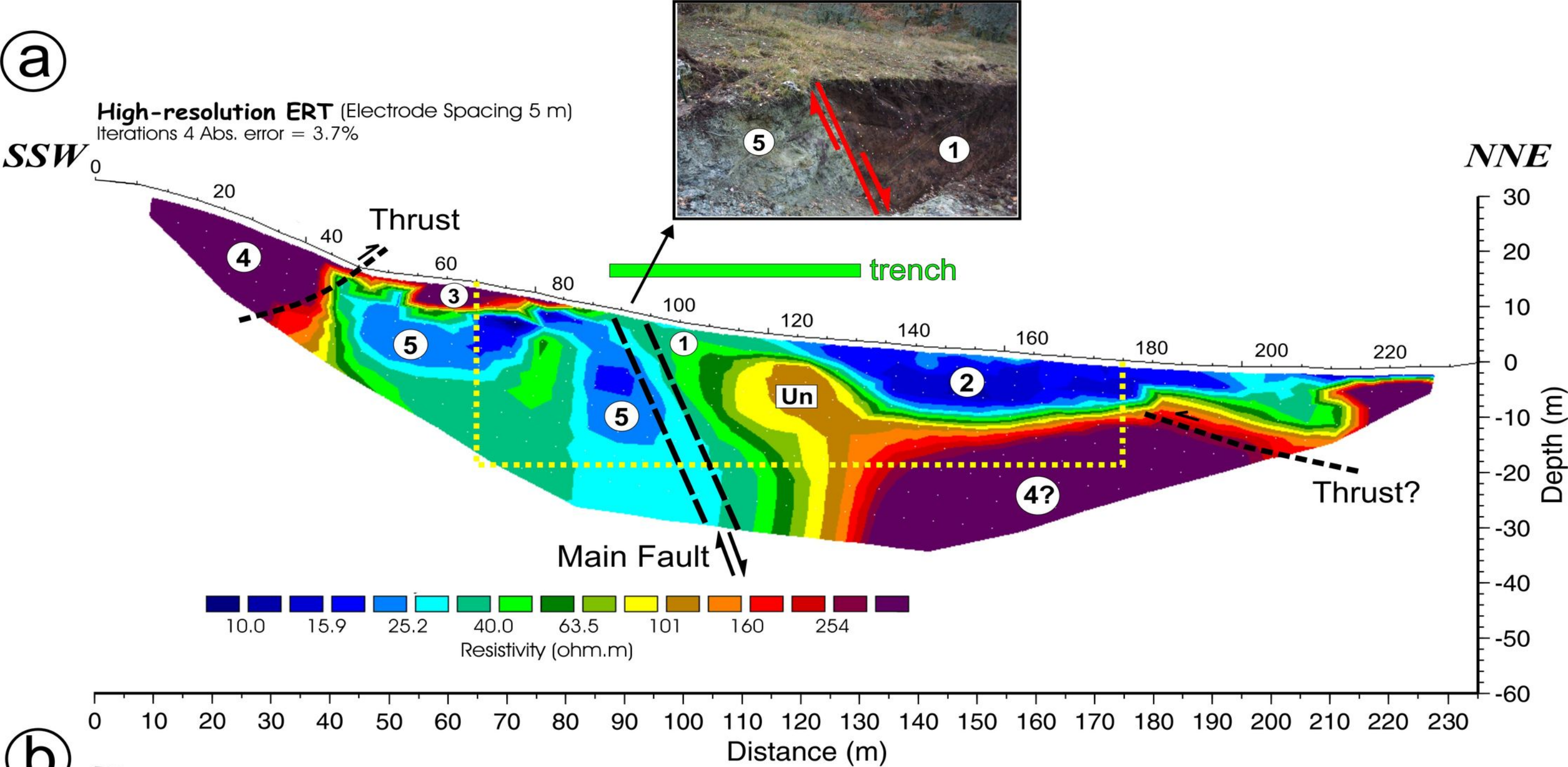


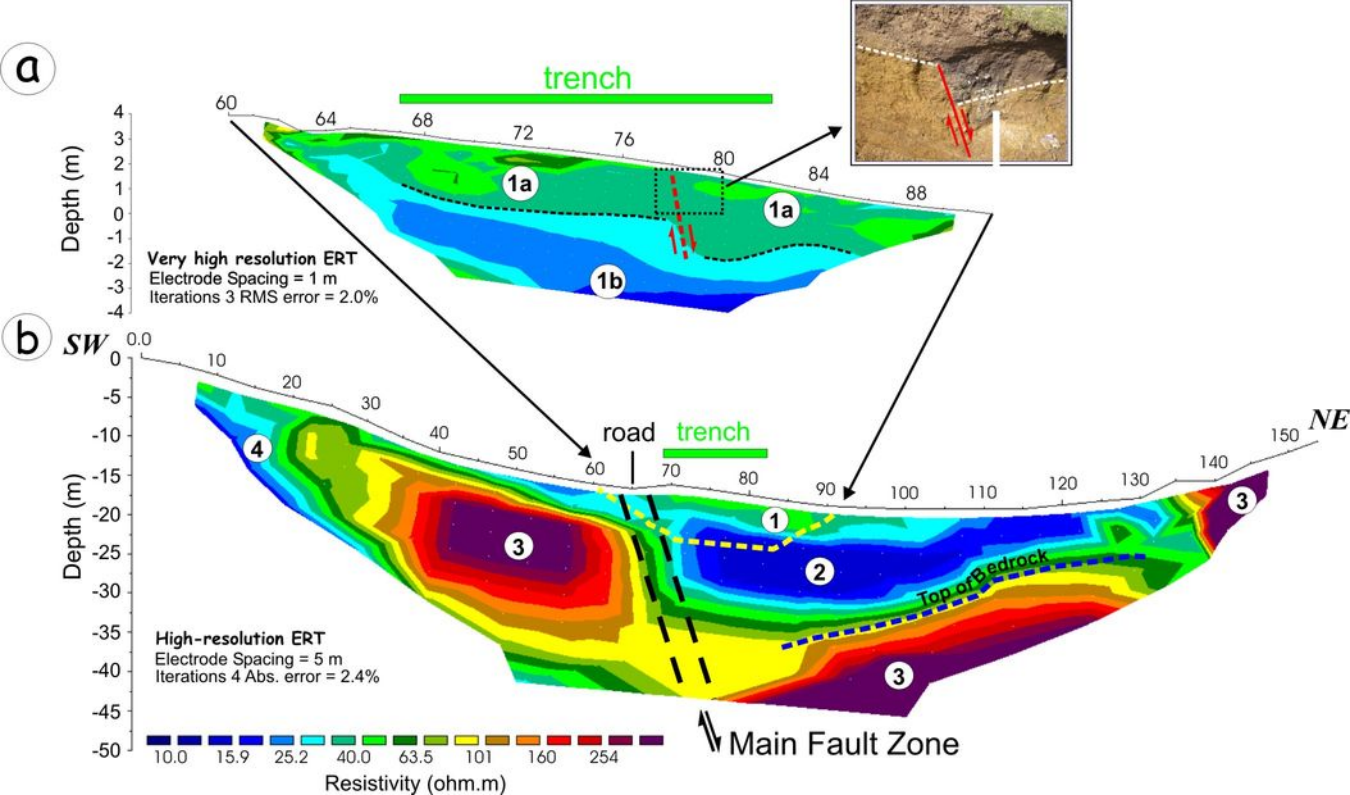


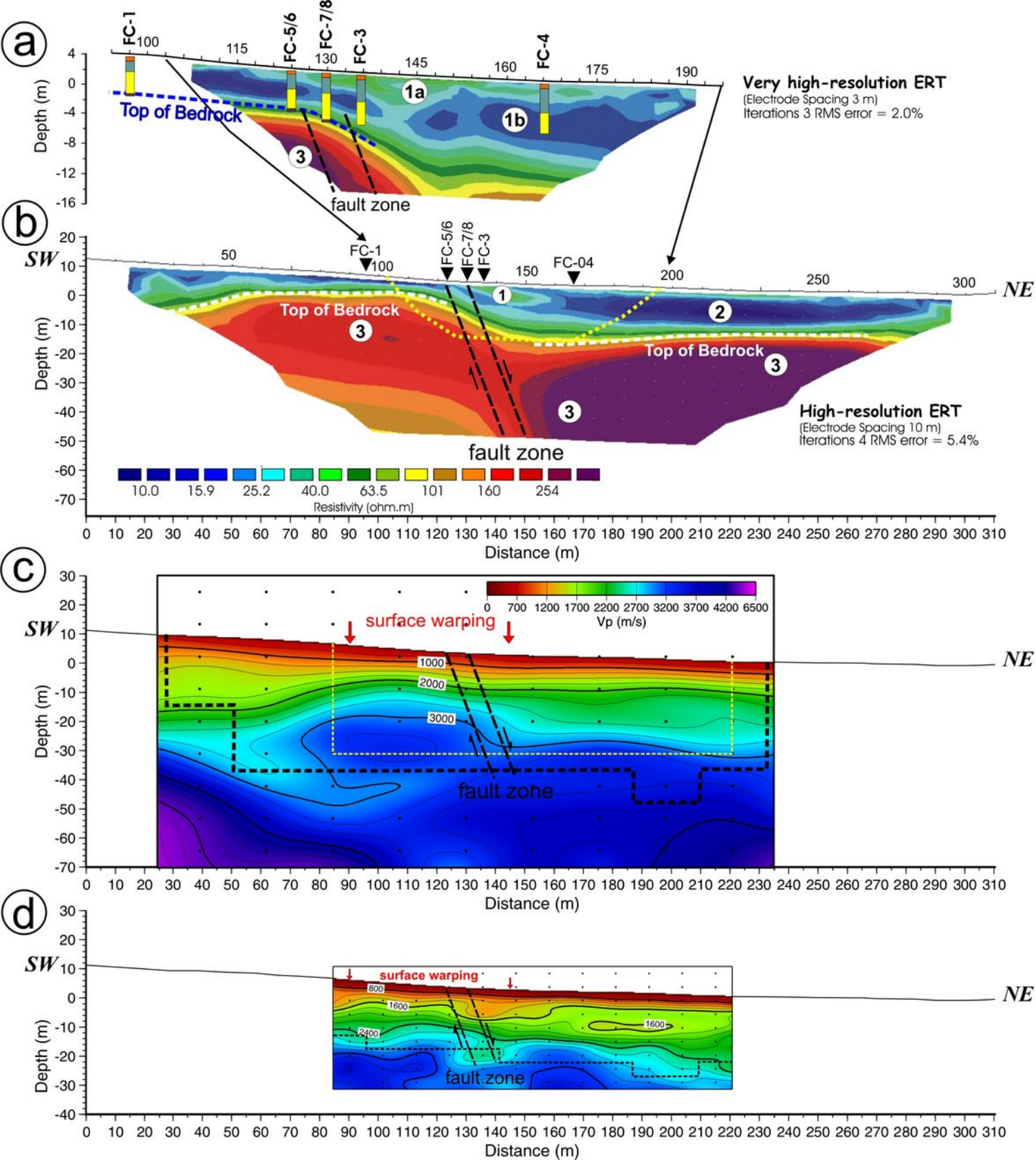


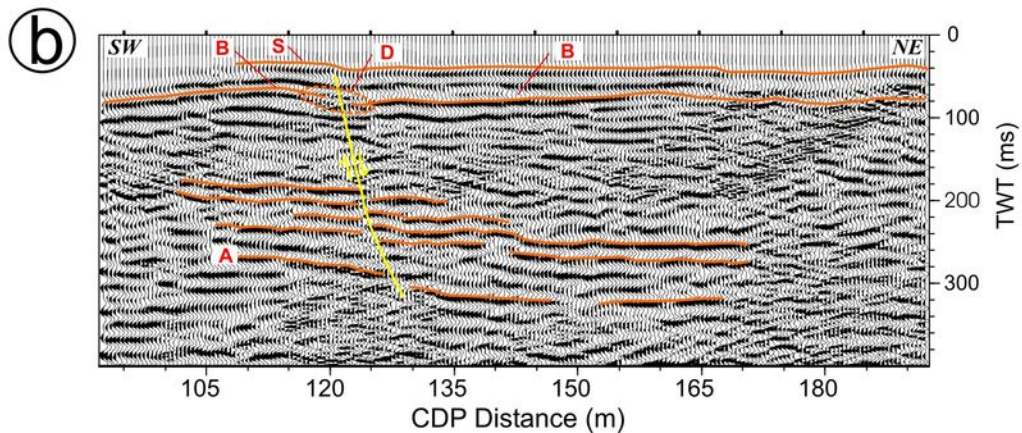
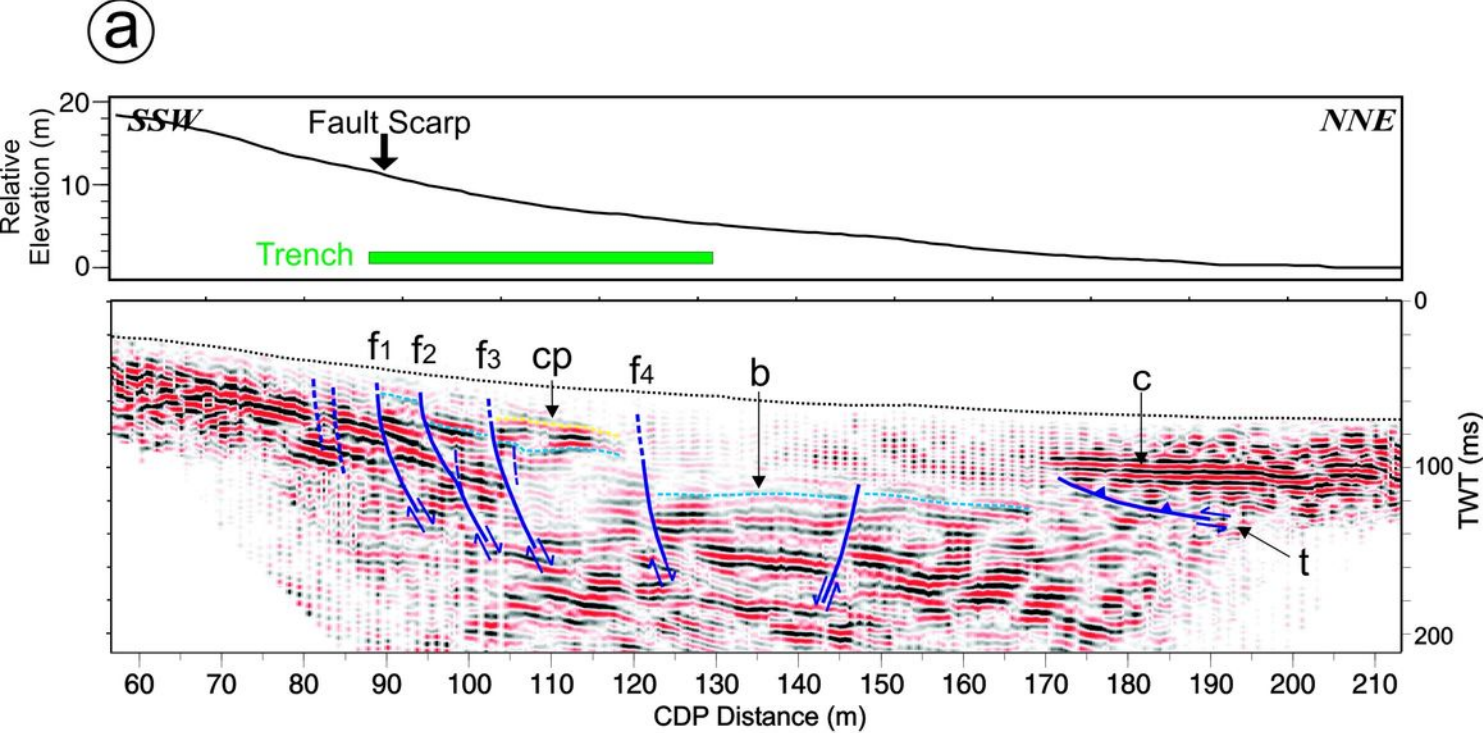
SCARP HEIGHT & OFFSET



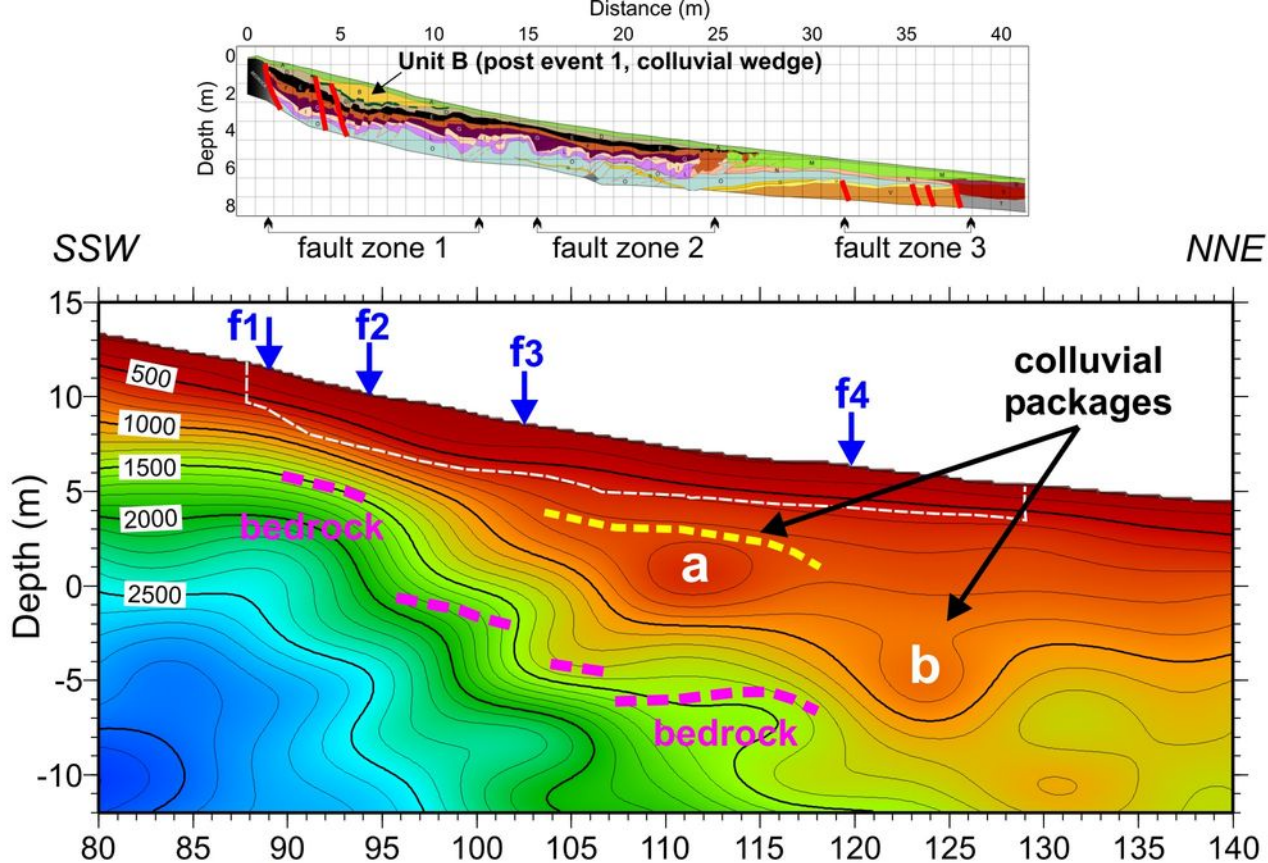




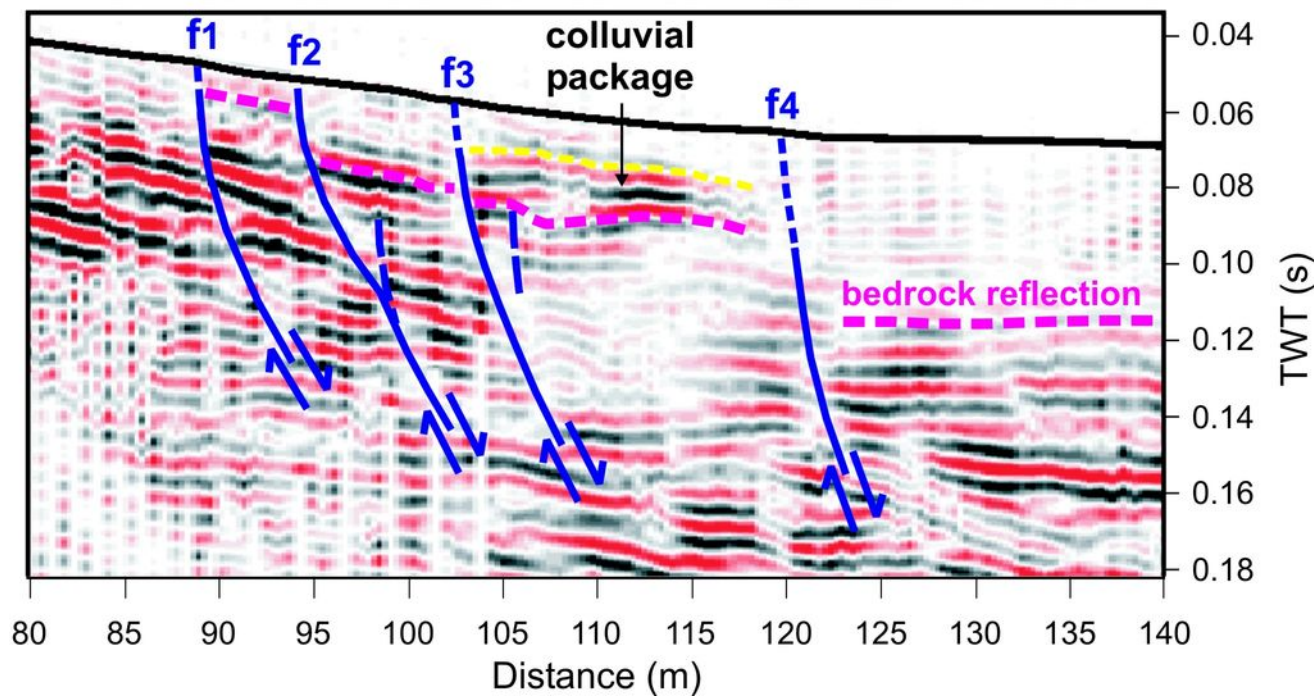


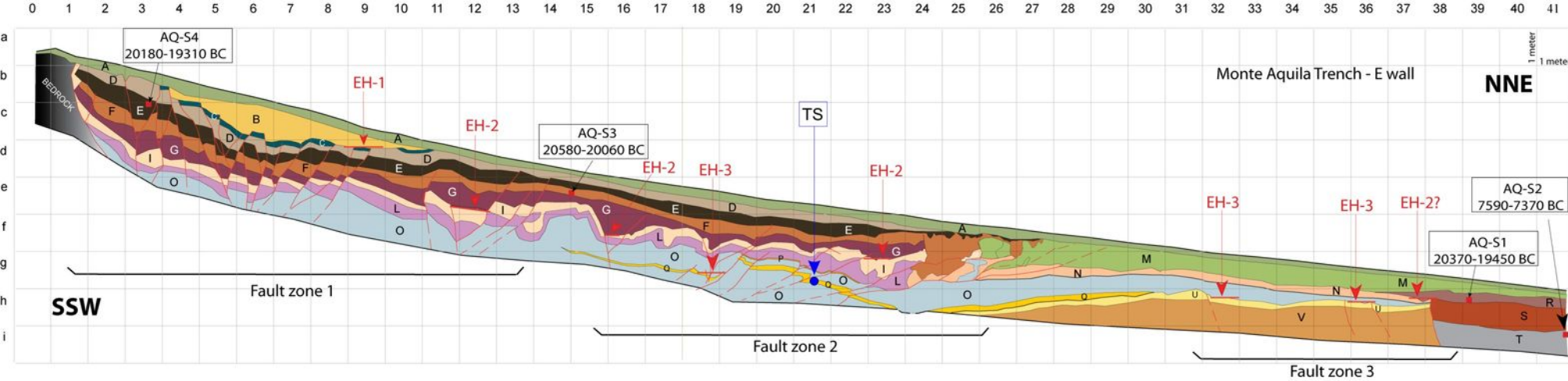


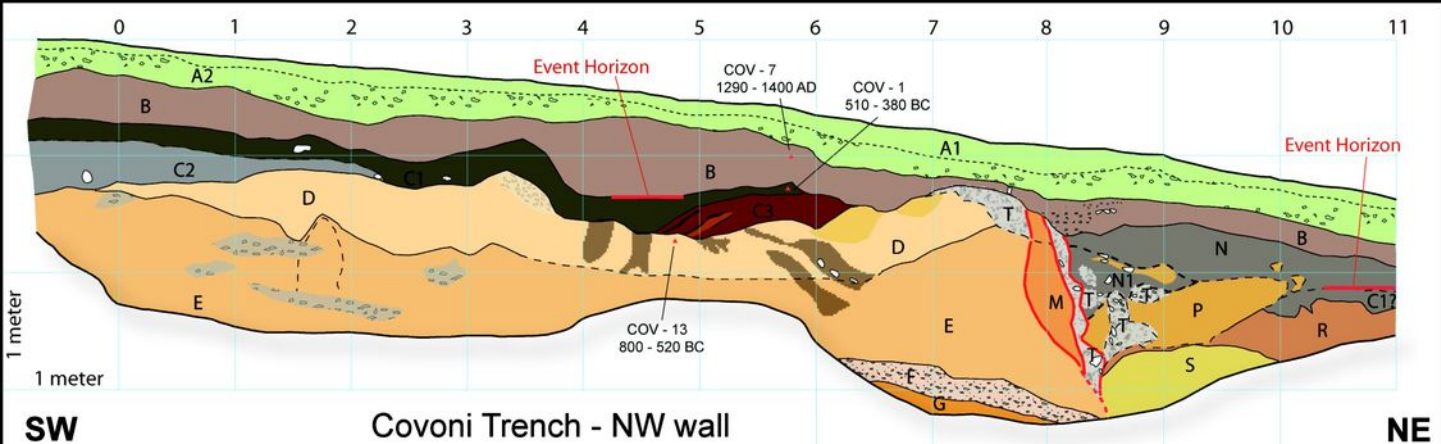
VHR Seismic Tomography

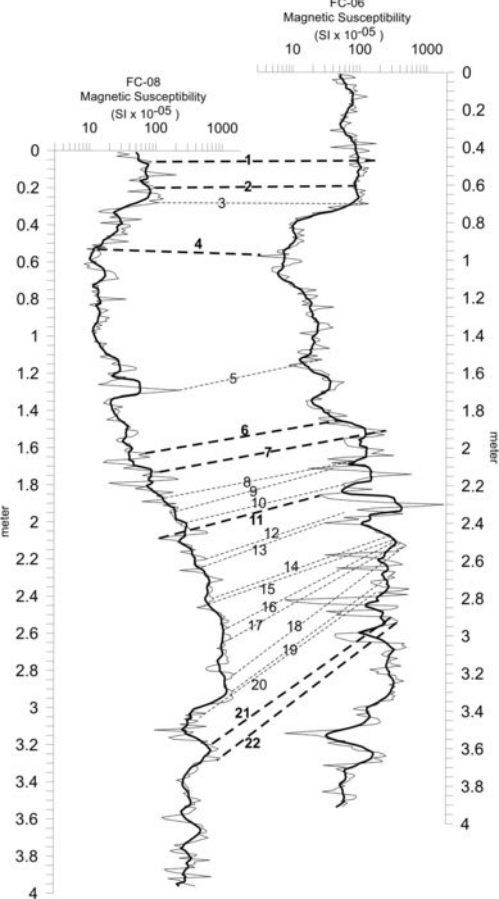


Stack Section

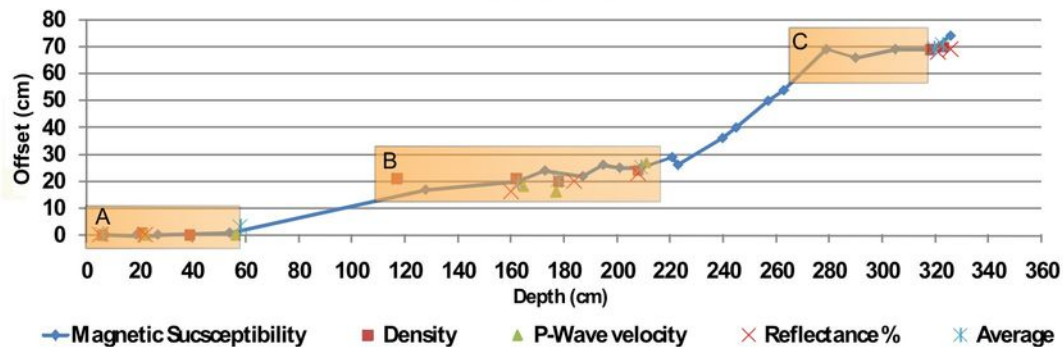








offset on FC-08



Electrical Resistivity Tomography					
Profile	Length (m)	Electrodes Number	Electrode Spacing (m)	Array Configuration	Model Depth (m)
Trincea HR	235	48	5	Wenner-Schlumberger	40
Covoni HR	155	32	5	Wenner-Schlumberger	25
Covoni VHR	31	32	1	Wenner-Schlumberger	6
Fornace HR	310	32	10	Dipole-Dipole	50
Fornace VHR	93	32	3	Dipole-Dipole	15

Dense Wide-Aperture Seismic Profiling (Seismic Tomography)						
Profile	Length (m)	Channels	Geophone spacing (m)	Source spacing (m)	Geophones Resonant Freq.	Source
Trincea	178	48	2,4	1	10 Hz	Rifle/Hammer
Fornace	210	48	4,6	1	10 Hz	Rifle

Small-offset Near-Vertical Seismic Reflection Profiling								
Profile	Length (m)	Channels (end-on geometry)	Near-trace offset (m)	Geophone spacing (m)	Source spacing (m)	Maximum Folding	Geophones Resonant Freq..	Source
Trincea	160	36	15	1	1	18	40 Hz	Rifle/Hammer
Fornace	100	36	15	1	1	18	40 Hz	Rifle

Table 1. Field parameters used for the ERT, the dense wide-aperture and the reflection seismic profiles at the three sites.

Table 2. Measured and calibrated ages (according to Calib REV5.0.2 by Stuiver and Reimer, 2005) of the samples collected in trenches.

Sample / Lab code	Type	Conventional age B.P.	13C/12C Ratio	Calibrated age 2 σ
AQ-S1 / Beta - 162075	Charcoal	18450 \pm 140	-24.5 0/00	20380-19460 BC
AQ-S2 / Beta - 162076	Charcoal	8480 \pm 50	-23.3 0/00	7590-7480 BC
AQ-S3 / Beta - 162077	Charcoal	18700 \pm 140	-24.6 0/00	20580-20060 BC
AQ-S4 / Beta - 162078	Charcoal	18280 \pm 110	-24.5 0/00	20190-19320 BC
COV-1 / Poz - 20853	Charcoal	2345 \pm 30	-24.2 0/00	510-380 BC
COV-7 / Poz - 20854	Charcoal	635 \pm 30	-26.4 0/00	1290-1400 AD
COV-13 / Beta - 233105	Charcoal	2530 \pm 40	-24.2 0/00	800-520 BC